HHS Public Access

Author manuscript

Nat Commun. Author manuscript; available in PMC 2015 January 31.

Published in final edited form as:

Nat Commun. ; 5: 4527. doi:10.1038/ncomms5527.

TRIP13 promotes error-prone nonhomologous end joining and induces chemoresistance in head and neck cancer

Rajat Banerjee[1], **Nickole Russo**[1], **Min Liu**[1], **Venkatesha Basrur**[2], **Emily Bellile**[6], **Nallasivam Palanisamy**[2,3], **Christina S. Scanlon**[1], **Elizabeth van Tubergen**[1], **Ronald C. Inglehart**[1], **Tarek Metwally**[1], **Ram-Shankar Mani**[2], **Anastasia Yocum**[2], **Mukesh K. Nyati**[4], **Rogerio M. Castilho**[1], **Sooryanarayana Varambally**[2,3], **Arul M. Chinnaiyan**[2,3,5], and **Nisha J. D'Silva**[1,2,3]

[1]Department of Periodontics and Oral Medicine, School of Dentistry, University of Michigan, Michigan, Ann Arbor, 48109

[2]Department of Pathology, University of Michigan, Michigan, Ann Arbor, 48109

[3]Michigan Center for Translational Pathology, University of Michigan, Michigan, Ann Arbor, 48109

[4]Department of Radiation Oncology, University of Michigan, Michigan, Ann Arbor, 48109

[5]Department of Urology, University of Michigan, Michigan, Ann Arbor, 48109

[6]Center for Cancer Biostatistics, University of Michigan, Michigan, Ann Arbor, 48109

Abstract

Head and neck cancer (SCCHN) is a common, aggressive, treatment-resistant cancer with a high recurrence rate and mortality, but the mechanism of treatment-resistance remains unclear. Here we describe a mechanism where the AAA-ATPase TRIP13 promotes treatment-resistance. Overexpression of TRIP13 in non-malignant cells results in malignant transformation. High expression of TRIP13 in SCCHN leads to aggressive, treatment-resistant tumors and enhanced repair of DNA damage. Using mass spectrometry, we identify DNA-PKcs complex proteins that mediate non homologous end joining (NHEJ), as TRIP13 binding partners. Using repair-deficient reporter systems, we show that TRIP13 promotes NHEJ, even when homologous recombination is intact. Importantly, overexpression of TRIP13 sensitizes SCCHN to an inhibitor of DNA-PKcs. Thus, this study defines a new mechanism of treatment resistance in SCCHN and underscores the

Correspondence to: Nisha J. D'Silva.

Correspondence and reprint requests should be addressed to: Nisha J. D'Silva, 1011 N. University Ave, Rm 5217, Dept of Periodontics and Oral Medicine, University of Michigan School of Dentistry, Ann Arbor, MI 48109-1078, Phone: (734) 764-1543, Fax: (734) 764-2469, njdsilva@umich.edu.

AUTHORS CONTRIBUTIONS

NJD conceived the project; NJD, RB, NLR designed experiments; RB, NLR, ML, VB, NP, CSS, EVB performed experiments; EB performed statistical analyses; NJD, RB, RSM, CSS, RI analyzed databases; NLR composed figures; RCI, TM helped in data analysis; VB, AY, RB analyzed mass spectrometry data; MKN helped with radiation experiments; RMC helped in comet assay; SV, AMC helped with data discussions; NJD, RB, NLR, CSS wrote the manuscript.

CONFLICT OF INTEREST

Dr Chinnaiyan is co-founder of Compendia Biosciences, which supports the Oncomine database used in this study. Neither Compendia Biosciences nor its subsidiary owner Life Technologies played any role in the design, conduct of this study, in the collection, analysis or interpretation of the data, or in the preparation, review or approval of the article. All other authors declare no conflict of interest in this manuscript.

importance of targeting NHEJ to overcome treatment failure in SCCHN and potentially in other cancers that overexpress TRIP13.

INTRODUCTION

Squamous cell carcinoma is a common cancer occurring in the head and neck, skin, esophagus, lung and cervix. Squamous cell carcinoma of the head and neck (SCCHN) is the sixth most common cancer globally [1]. Half of the 600,000 patients diagnosed annually will die in 5 years [1, 2]. The morbidity is worse than breast cancer or melanoma [2] due to late diagnosis and tumor relapse. Late-stage lesions are treated by chemotherapy and radiation, which has changed little in 50 years, emphasizing the need for new treatment [1]. Characterization of the mechanism that promotes treatment-resistance will provide novel treatment targets.

Although the mechanism is unclear, pathways that promote DNA-repair induce treatment-resistance [3], underscoring the importance of characterizing these proteins in SCCHN. Double-strand breaks (DSBs), the most dangerous type of DNA damage, are induced by radiation and chemotherapy [4] and DSBs are repaired primarily by homologous recombination (HR) or NHEJ [3]. HR requires a DNA template, normally a homologous chromosome in germ cells or a sister chromatid in somatic cells. HR is essential for genetic diversity and transmission of genetic information between generations of cells and organisms. NHEJ occurs throughout the cell-cycle and is required for physiologic processes including antigen receptor diversity and generation of antigen-specific antibodies [5]. NHEJ is usually inaccurate since DNA ends join without a template [6]. Error-prone or excessive repair promotes mutations, chromosome instability and cancer whereas unrepaired DNA leads to cell death. In cancer, efficient repair of radiation- and chemotherapy-induced DSBs promotes treatment-resistance with subsequent relapse. Therefore, inhibition of NHEJ would improve response to treatment.

Based on meta-analyses of multiple SCCHN datasets, we nominated Thyroid hormone Receptor Interactor 13 (TRIP13 or HPV16E1BP) as an oncogene. TRIP13 is the mouse ortholog of pachytene checkpoint 2 (Pch2), a checkpoint for synapsis prior to DSB repair and recombination in yeast and C. elegans [7, 8]. In mice, TRIP13 mediates DSB-repair [9, 10], however TRIP13's role in humans has not been investigated. In this study, we investigated a mechanism by which TRIP13 promotes treatment-resistance. Overexpression of TRIP13 in non-malignant cells leads to malignant transformation. High expression of TRIP13 in SCCHN promoted aggressive tumor growth, treatment-resistance, and enhanced repair of DNA damage. TRIP13 binding partners, including DNA-PKcs complex proteins mediating NHEJ, were identified by mass spectrometry. Repair-deficient reporter systems revealed that TRIP13 promotes NHEJ. Overexpression of TRIP13 sensitized SCCHN to an inhibitor of DNA-PKcs and mpairment of TRIP13 ATPase activity diminishes its DSB repair efficiency. These findings define a mechanism of treatment resistance in SCCHN and emphasize the importance of targeting NHEJ to overcome treatment failure.

RESULTS

TRIP13 is overexpressed in SCCHN

Recent sequencing studies emphasized the limited number of mutations present in SCCHN [11]. Therefore, we performed meta-analysis of multiple SCCHN datasets (Fig. 1A, left to right: Cromer Head-Neck, accession GSE2379[12], Estilo Head-Neck, accession GSE13601[13], Ye Head-Neck, accession GSE9844[14], Kuriakose Head-Neck, accession GDS2520[15], Ginos Head-Neck[16], Toruner Head-Neck, accession GSE3524[17], all available from Oncomine, Compendia Bioscience, Ann Arbor, MI), to nominate potential novel oncogenes. *TRIP13* was significantly upregulated in all six datasets interrogated (Fig 1A). The Cancer Genome Atlas (TCGA) dataset showed highly increased *TRIP13* copy number (~4 copies) in ~14% (40/290) of SCCHN patients (Fig 1B). *TRIP13* was nominated as an oncogene and is not mutated in SCCHN (Supplementary Fig 1A, left panel). *TRIP13* copy number and gene expression frequency are increased in multiple cancers (Supplementary Fig 1A, middle and right panels). Compared to immortalized non-malignant keratinocytes, fluorescence-in-situ-Hybridization (FISH) showed increased *TRIP13* copy number in SCCHN cells and tissue (Fig 1C, Supplementary Fig 1B, 1C).

SCCHN exhibited high TRIP13 expression in tumor tissue compared to adjacent normal mucosa in paired normal and cancer tissue specimens (Fig 1D and bottom graph). In a TMA, the intensity and proportion of TRIP13 were significantly higher in the nuclei in SCCHN compared to normal oral mucosa (Fig 1E, clinical data in Supplementary Table I). Together, these data indicate that TRIP13 is upregulated in SCCHN patients due to gene amplification.

TRIP13 promotes proliferation invasion and cell survival

TRIP13 mRNA and protein expression were verified by Q-RT-PCR (Fig 2A) and immunoblot (Fig 2B) in SCCHN cell lines. In ten of twelve SCCHN cell lines, TRIP13 was upregulated compared to non-malignant keratinocytes (HOK and HOK16B).

Although expression data suggested that *TRIP13* is overexpressed in SCCHN, the role of *TRIP13* is unknown. Hence, we investigated the function of TRIP13 in SCCHN progression by performing proliferation, invasion and survival assays. In initial studies four different siRNAs against TRIP13 were evaluated (Supplementary Fig 1D, 1E) in UM-SCC-22B and OSCC3, which have high endogenous TRIP13 (Fig 2B). The siRNAs (si6, si8) showing the most sustained knockdown of TRIP13 (Fig 2C) were used for proliferation and invasion studies. Downregulation of TRIP13 significantly decreased proliferation (Fig 2D) and invasion (Fig 2E). Similar findings were observed in OSCC3 (Supplementary Fig 2A through 2C) and UM-SCC-5 (Supplementary Fig 3A through 3C), two independent cell lines, which also overexpress TRIP13. si6 had a profound early effect on downregulation of TRIP13 (Supplementary Fig 1E), but downregulation was more sustained with si8 (Fig. 2C) across cell lines, likely due to apoptosis of cells transfected with si6. Hence, si8 was used for subsequent studies.

To understand the impact of TRIP13 on cell survival, apoptosis was evaluated by flow-cytometry in cells stained with FITC-Annexin V and Propidium Iodide (PI). Downregulation of TRIP13 significantly increased apoptosis in UM-SCC-22B (Fig 2F),

OSCC3 (Supplementary Fig 2D) and UM-SCC-5 (Supplementary Fig 3D). DNA fragmentation of apoptotic cells was visualized with fluorescein-labeled Brd-UTP (terminal deoxynucleotidyl transferase dUTP nick-end labeling-TUNEL) and quantified (Fig 2G, Supplementary Figs 2E and 3E). To understand whether knockdown of TRIP13 impacts the cell cycle, SCCHN cells were synchronized, stained with PI and analyzed by flow-cytometry. Knockdown of TRIP13 led to fewer cells in the G1- and S-phases and more in the G2-phase (Fig 2H, Supplementary Fig 2F). Cells arrested in G2 progress to apoptosis instead of moving into the M-phase [18]. Together these findings suggest that TRIP13 promotes oncogenic phenotypes *in-vitro*.

TRIP13 promotes tumor progression

To investigate the function of TRIP13 *in-vivo*, we attempted to generate SCCHN cell lines with stable downregulation of TRIP13. However, repeated attempts to generate these cells were unsuccessful, likely due to apoptosis. Using a different approach, we generated doxycycline-inducible shTRIP13- and control-SCCHN cell lines by transducing TRIPZ-shTRIP13 and shTRIPZ-control lentiviral particles in UM-SCC-22B and OSCC3. Mixed clonal populations were selected against puromycin. Knockdown was verified by immunoblot (Fig 3A, Supplementary Fig 4A respectively) and proliferation (Fig 3B, Supplementary Fig 4B) assays. UM-SCC-22B-shTRIPZ-shTRIP13 (shTRIP13) and control (shControl) cells were injected subcutaneously in mice (n=10). After 8d, similar-sized tumors appeared in both shcontrol and shTRIP13 groups and doxycycline administration was initiated (n=5) in one and no-doxycycline was administered in the other group (n=5). The impact of doxycycline administration on tumor growth was rapid. Doxycycline-induced shTRIP13 significantly arrested tumor growth compared to doxycycline-treated control tumors (Fig 3C, 3D). Tumor volume (Fig 3E) and weight (Fig 3F) were significantly less for doxycycline-induced shTRIP13. No significant difference in tumor size was observed in mice not administered doxycycline (Supplementary Fig 4C, 4D). Proliferation and survival of tumor cells were investigated in these tumors; doxycycline-treated shTRIP13 tumors had significantly less mitoses (Fig 3G), a marker of proliferation, and higher apoptosis (Fig 3H), than corresponding control tumors. Furthermore, angiogenesis was quantified on tissue sections from CAM tumors generated from doxycycline-induced TRIP13 knockdown (TripZ) and control UM-SCC-22B cells. No significant difference in vessel length and number of junctions was observed (Supplementary Fig 4E), suggesting that TRIP13 does not regulate angiogenesis. Together the *in-vitro* and *in-vivo* results support a tumorigenic role for TRIP13.

To establish an oncogenic role, we interrogated whether TRIP13 could transform non-malignant cells using the focus formation (transformation) assay in NIH3T3 fibroblasts. NIH3T3 cells grow to confluence and senesce since contact inhibition prevents cell stratification [19]. However, overexpression of TRIP13 in NIH3T3 cells (Fig 3I) led to significantly more cellular stratification, i.e. focus formation (Fig 3J), and proliferation (Fig 3K) than control NIH3T3-pCMV6 cells. To conclusively establish the oncogenicity of TRIP13, tumor growth of NIH3T3-TRIP13 cells was verified *in-vivo* using the chick chorioallantoic membrane (CAM) assay. After 3d, GFP-labeled NIH3T3-TRIP13 cells formed a three-dimensional tumor (Fig 3L; n=5; broken lines) in contrast to the thin-layer of

control cells. NIH3T3-TRIP13 cells invaded the underlying mesenchymal tissue (Fig 3M, lower panel, arrowheads and graph) in contrast to control (NIH3T3-pCMV6) cells, which remained as a single layer on the surface of the CAM (Fig 3M, upper panel and graph).

In a complementary approach TRIP13 was stably overexpressed in UM-SCC-1, a cell line with low endogenous TRIP13 (Fig 2B). Overexpression was verified by immunoblot (Fig 4A). UM-SCC-1-TRIP13 cells exhibited significantly higher proliferation (Fig 4B), invasion (Fig 4C) and migration (Fig 4D,) compared to control (UM-SCC-1-pCMV6) cells. To investigate the *in-vivo* impact of overexpression of TRIP13, cells were injected subcutaneously in mice (n=10) and tumors were grown until mice became moribund. Control tumors (UM-SCC-1-pCMV6) (Fig 4E, pCMV6, n=5) grew significantly slower than TRIP13 overexpressing tumors (UM-SCC-1-TRIP13) (Fig 4F, TRIP13, n=5). Moreover, mice with TRIP13 tumors had poorer survival than those with control tumors (Fig 4G; p=0.0019, log-rank). This correlated with significantly increased tumor size (Fig 4H). Tissue sections and immunohistochemical staining were used to determine the mitotic index and proliferating cell nuclear antigen (PCNA)-positive cells, respectively, both measures of proliferative activity. UM-SCC-1-TRIP13 tumors had significantly more mitoses (Fig 4I), a higher proliferative index (Fig 4J), and a lower apoptotic index (Fig 4K) than control tumors, consistent with our *in-vitro* findings that TRIP13 promotes survival. Together the *in-vitro* and *in-vivo* studies establish *TRIP13* as an oncogene.

TRIP13 mediates treatment-resistance

Given the role of TRIP13 in promoting cell survival, we investigated its effects in response to cisplatin (CDDP) chemotherapy and ionizing radiation (IR)-induced cell death. In initial studies, the IC_{50} for CDDP in UM-SCC-22B and OSCC3 were determined to be 5μM and 2μM, respectively (Supplementary Figs 4F, 4G, respectively). UM-SCC-22B (Fig 5A) and OSCC3 (Supplementary Fig 5A) cells with downregulated TRIP13 were treated with CDDP and cell number was counted. Cells treated with siTRIP13+CDDP grew significantly slower than control siNT+CDDP, suggesting a role for TRIP13 in chemoresistance. The inhibitory effect of siTRIP13 was greater than that of CDDP; combination treatment (siTRIP13+CDDP) had an additive effect. Clonogenic assays showed that survival of siTRIP13+IR cells was significantly less than control NT+IR cells (Fig 5B, Supplementary Fig 5B), consistent with a role for TRIP13 in promoting IR-resistance. DNA fragmentation, a marker of apoptosis, was greater in siTRIP13+IR than control NT+IR cells (Fig 5C, Supplementary Fig 5C).

Ionizing radiation and CDDP promote apoptosis by inducing DSB, the most lethal form of DNA damage [4]. Therefore, we investigated the effects of TRIP13 on DSB-repair. Since histone H2AX is phosphorylated at Ser-139 (γH2AX) in response to DSBs [20], γH2AX expression was used to quantify DSBs. Loss of γH2AX indicates efficient DSB-repair whereas persistent γH2AX indicates impaired DSB-repair [21]. In irradiated UM-SCC-22B and OSCC3, knockdown of TRIP13 correlated with γH2AX accumulation (Fig 5D, Supplementary Fig 5D, respectively). Spontaneous DSBs and DNA-repair occur during cell proliferation. Therefore, we investigated DSBs in cells transfected with NT and siTRIP13 and observed significantly more γH2AX foci/cell in siTRIP13- than NT-cells (Fig 5E,

Supplementary Fig 5E). These studies suggest that loss of TRIP13 promotes accumulation of DNA damage. Hence, we evaluated the impact of TRIP13 on DSB by the comet assay in NT- and siTRIP13-cells (Fig 5F, Supplementary Fig 5F). Cells with siTRIP13 showed significantly increased DNA damage in UM-SCC-22B (Fig 5G) and OSCC3 (Supplementary Fig 5G). To determine whether siTRIP13-mediated DSB induces apoptosis or apoptosis induces DSB, we performed a time course experiment to investigate the sequence between γH2AX and apoptosis after knockdown of TRIP13 (Fig 5H). We observed that γH2AX (marker of DSBs) precedes PARP cleavage (marker of apoptosis). γH2AX was observed in siTRIP13 cells as early as 4hr post-transfection whereas cleaved-PARP appeared at 24hr post-transfection indicating siTRIP13 mediated DSB precedes apoptosis (Fig 5H). Taken together, these studies support that TRIP13 promotes treatment-resistance via enhanced DNA-repair.

TRIP13 has an ATPase domain, a hallmark of AAA-ATPase proteins [22] which mediate protein-DNA or protein-protein complex assembly [23]. To identify proteins that interact with TRIP13, we performed LC-tandem mass spectrometry [24]. Flag-tagged-TRIP13 was purified with Sigma-Flag-Beads (M2) from UM-SCC-1 cells stably overexpressing FLAG-TRIP13, , stained and immunoblotted (Supplementary Fig 6A). Interacting proteins were identified using X!Tandem/Trans-Proteomic Pipeline software [25]. Proteins with a Protein Prophet probability score >0.9 (error rate<2%) were considered positive identifications and functionally classified (Supplementary Table 2). These proteins were entered in the string database (http://string-db.org/) to predict the interaction network. Molecules out of the network were deleted and an interaction map consisting of 18 molecules is summarized (Fig 6A). The greatest interaction network concepts determined from KEGG pathway analysis were NHEJ and Cell cycle/DNA-repair pathways (Supplementary Table 3). NHEJ/DNA-repair group proteins included KU70 (XRCC6), KU80 (XRCC5) and DNA-PKcs (PRKDC) (Fig 6A). Mass spectrometry sequence coverage of these interacting proteins is shown (Fig 6B). The interactions were further validated by immunoprecipitation with TRIP13 antibody in UM-SCC-22B (Fig 6C) and OSCC3 (Supplementary Fig 6B). KU70, KU80 and DNA-PKcs co-immunoprecipitated with TRIP13 but not control IgG (Fig 6C, Supplementary Fig 6B). To verify that TRIP13 interacted with each protein directly, not via DNA, immunoprecipitation was also performed in the presence of ethidium bromide. In a complementary experiment, KU70, KU80 and DNA-PKcs were immunoprecipitated with corresponding antibodies and immunoblotted with TRIP13 antibody. TRIP13 co-immunoprecipitated with each of these proteins but not with control IgG (Fig 6D, Supplementary Fig 6C), confirming interaction with DNA-repair proteins in SCCHN.

DSBs are primarily repaired by accurate HR or error-prone NHEJ. Since KU70, KU80 and DNA-PKcs are members of the NHEJ repair complex [4], we investigated the involvement of TRIP13 in NHEJ using reporter constructs [26] in the host cell reactivation system of HCC1937, a BRCA1 mutant cell line. The absence of BRCA1 in these cells inhibits HR, leaving NHEJ as the default repair pathway. HCC1937 cells stably transfected with NHEJ (Fig 6E) or HR (Fig 6F) reporter constructs () were transiently transfected with NT or siTRIP13. 48h later, the cells were co-transfected with the rare cutting endonuclease I-SceI expression plasmid and a transfection efficiency control plasmid (pDsRed2-N1), and 72h later were analyzed by flow cytometry. The I-SceI endonuclease induces DSBs in the

reporter GFP cassette (schematics in Supplementary Fig 6D, 6E). When the two ends of the DSB are joined by NHEJ or HR, GFP is expressed. The relative efficiency of DSB-repair was calculated as the ratio of GFP+/DsRed+ cells. GFP-expression was significantly decreased in HCC1937-NHEJ-siTRIP13 compared to HCC1937-NHEJ-siNT (Fig 6E), consistent with a role for TRIP13 in NHEJ. As a negative control for these HR deficient cells, siTRIP13 had minimal impact on HR reporter expression (Fig 6F).

To verify that TRIP13 facilitates NHEJ, a mini-NHEJ assay was performed with linearized plasmid with non-cohesive ends. In this assay (See supplementary Fig 7A), recircularization of linearized plasmid occurs via NHEJ due to the absence of DNA template necessary for HR. Mini-NHEJ extracts from UM-SCC-22B and OSCC3 with siTRIP13 or siNT were incubated with linearized plasmid and recircularization was evaluated on agarose gels (Fig 6G, Supplementary Fig 6F respectively) followed by transformation into competent bacteria and colony-counting. When incubated with extracts from siTRIP13 cells, recircularized plasmid was undetectable and the number of colonies was reduced compared to siNT (Fig 6G, Supplementary Fig 6F). Recircularization of plasmid DNA was confirmed by generating PCR-product from the primers P1-Forward and Reverse (Supplementary Table 4) (Supplementary Fig 7A, 7B) and sequence-confirmation of base loss in NHEJ (Supplementary Fig 7C). Moreover a semi-quantitative PCR of 15-cycles showed reduced rejoined products when the rejoining reaction was performed with siTRIP13- versus NT-extracts from three SCCHN cell lines (Supplementary Fig 7D). Together these findings show that TRIP13 is involved in the NHEJ pathway.

HR-pathway protein RAD51 translocates from the cytoplasm to the nucleus to accumulate at DSBs. To investigate the involvement of TRIP13 in HR, γH2Ax/Rad51 co-localization foci were quantified in UM-SCC-22B. TRIP13 expression was inversely correlated with γH2AX/Rad51 co-localization (Fig 6H), suggesting that in HR-competent cells, DSB-repair defaults to the HR pathway when TRIP13 is downregulated. Similar results were obtained with OSCC3 (Supplementary Fig 8A). Together our findings show that TRIP13 promotes NHEJ in HR-competent cells and that HR occurs when TRIP13 is downregulated.

Induction of the NHEJ pathway confers treatment resistance making DNA-PKcs an attractive target in clinical trials[27]. After establishing that overexpression of TRIP13 drives treatment resistance via NHEJ, we hypothesized that SCCHN cells overexpressing TRIP13 would be more sensitive to a DNA-PKcs inhibitor than cells with low expression of TRIP13. To investigate this possibility, UM-SCC-1-pCMV6 and UM-SCC-1-TRIP13 cells were treated with multiple concentrations of NU7026 (100nM to 10μM, Supplementary Fig 8B, 8C), a DNA-PKcs inhibitor. DNA-PKcs autophosphorylation at Ser 2056 and proliferation were assessed. Control cells were less sensitive to NU7026 with respect to inhibition of DNA-PKcs phosphorylation and proliferation (Supplementary Fig 8B, 8C, left panels, respectively) than TRIP13 overexpressing cells (Supplementary Fig 8B, 8C, right panels, respectively). Furthermore, cells overexpressing TRIP13 (UM-SCC-1-TRIP13) were more sensitive to NU7026, with an IC_{50} of 10μM compared to 13μM for control cells (Fig 7A). To determine the effects on proliferation, UM-SCC-1-TRIP13 and UM-SCC-1-pCMV6 cells were treated with NU7026 (Fig 7B). Using a mixed-effects model to account for correlation among repeat measurements, we observed the difference in mean slope over time

with and without NU7026 in Control- versus TRIP13-overexpressing groups. Importantly, the differences in slopes for the TRIP13 group (+/− NU7026), were significantly larger than the differences between control-pCMV6 cells (Fig 7B), confirming that high expression of TRIP13 increases sensitivity to the NHEJ inhibitor. In addition, when NHEJ is blocked with NU7026, Rad51/γH2AX foci increased significantly (Fig 7C). Importantly, similar results were observed *in-vivo*. In the CAM, NU7026-mediated inhibition of tumor growth and metastasis was greater with TRIP13 than control cells. UM-SCC-1-pCMV6 cells +/− NU7026 exhibited no significant difference in tumor size (Fig 7D,), whereas NU7026 significantly inhibited growth of UM-SCC-1-TRIP13 tumors (Fig 7E). More importantly metastasis of these cells to the lower CAM, as detected by fluorescence microscopy (Fig 7F, left panel) and quantitative ALU-PCR for Lower CAM and liver [28] (Fig 7F, right top and bottom panels, respectively), was inhibited by NU7026. Together these data show that TRIP13 promotes DSB repair and treatment resistance via the NHEJ pathway. Importantly, by favoring NHEJ, TRIP13 inhibits the intact HR pathway in SCCHN.

TRIP13 has an ATPase domain, a hallmark of AAA-ATPase proteins [22] which mediate protein-DNA or protein-protein complex assembly [23]. To determine whether the ATPase activity mediates the oncogenic activity of TRIP13, we generated TRIP13 mutants by altering amino acids at the conserved Walker A motif by site-directed mutagenesis or by deleting the conserved ATPase domain (Fig 8A). The Walker A motif is required for ATP-binding activity [29]. The ATPase domain is required for diverse activities of AAA-ATPase proteins [30]. Expression of TRIP13^{mt} (TRIP13^{G184A}) and TRIP13$^{\Delta mt}$ (TRIP13$^{\Delta 293–312}$) mutant proteins was verified after transient transfection in COS-1 (Fig 8B). ATPase enzymatic activity, assessed using the malachite green ATPase assay, was deficient with both mutant constructs when compared to wild type TRIP13 (Fig 8C). The deficiency of the ATPase activity also impaired proliferative activity (Fig 8D). Similar findings were observed in UM-SCC-1 (Fig 8E through 8G). Moreover, in TRIP13 overexpressing cells the low γH2AX is consistent with more efficient DSB repair compared to control pCMV6 cells (Fig 8H lane 2 compared to lane 1). TRIP13-mediated repair was impaired when the ATPase domain was mutated (Fig 8H lanes 3 and 4 compared to lane 2). The loss of ATPase activity also impaired TRIP13-mediated tumor growth on the CAM (Fig 8I and 8J).

DISCUSSION

Chemotherapy and radiation are current treatment options for advanced SCCHN [31]. Resistance to treatment is correlated with recurrence and morbidity, underscoring the importance of developing new treatment strategies. Here we report that TRIP13 sensitizes SCCHN to a DNA-PKcs inhibitor. TRIP13 was designated as an oncogene by meta-analysis of several gene expression datasets and functionally validated as an oncogene by malignant transformation of non-malignant cells, tumor growth and invasion assays. Several NHEJ proteins were identified as binding partners of TRIP13, suggesting a role for TRIP13 in NHEJ, which was verified by multiple robust approaches. Consistent with the correlation between NHEJ and treatment-resistance [27], SCCHN cells overexpressing TRIP13 are resistant to chemotherapy and radiation but responsive to NHEJ inhibitors. Our studies define a mechanism of treatment resistance in cancer and emphasize the importance of targeting NHEJ to overcome treatment resistance in SCCHN overexpressing TRIP13.

TRIP13 has not been investigated as an oncogene although it is overexpressed in multiple cancers [32, 33, 34, 35]. The *TRIP13* gene is amplified in early-stage non-small-cell-lung cancer [33]. In a comparative genomic hybridization screen of 19 tumors, *TRIP13* amplification was identified in 68% of tumors. We observed amplification of TRIP13 by FISH in ~15% of SCCHN, suggesting additional regulatory mechanisms. Using a bioinformatics approach, increased TRIP13 transcript and protein correlated with prostate cancer progression[36]. Another study reported overexpression of TRIP13 in a cutaneous lymphoma [37]. Prior to our study, the oncogenic role of TRIP13 had not been investigated. Although TRIP13's function was unknown in humans, it has been investigated in mice, yeast and worms. In mice, TRIP13 is essential for non-crossover recombination during DSB-repair but not at synaptic checkpoints during meiosis [10, 38, 39]. DSB-repair occurs primarily via HR in germ cells and via NHEJ in somatic cells [40]. Our studies strongly support a role for TRIP13 in DSB-repair via NHEJ. Previous studies showed that the role of *TRIP13* varies between species. In yeast, worms and D. melanogaster, *Pch2*, the *TRIP13* ortholog, is part of the synapsis checkpoint in germ cells [7, 8, 41]. In yeast, Pch2 is required for checkpoint arrest during defective recombination and synapsis [42]. Spermatocyte and oocyte death are observed in pachynema and birth in TRIP13 mutant mice. Although spermatocytes synapse completely, there is an accumulation of Rad51 [10]. A recent network analysis of protein-protein interactions in mitosis suggested that TRIP13 is a kinetochore protein that interacts with the mitotic spindle but this was not experimentally verified [35]. Our data in SCCHN establish a role for TRIP13 in NHEJ.

In humans, *TRIP13* is located at chromosome 5p15 and encodes a protein of 432 amino acids. TRIP13 belongs to the AAA+ATPase family of chaperone proteins that facilitate assembly or degradation of protein complexes that regulate diverse cellular functions [22]. Hence, we investigated the binding partners of TRIP13 and identified the association of TRIP13 with repair proteins including KU70, KU80 and DNA-PKcs. During NHEJ, KU70 and KU80 form a heterodimer at the free DNA ends and recruit and activate DNA-PKcs, the catalytic subunit of DNA-dependent protein kinase [43]. Other members subsequently recruited to this DNA-PK complex include artemis, XRCC4 and DNA ligase IV. Our data also supports the functional effect of TRIP13 ATPase activity. Given its role as an ATPase, it is possible that TRIP13 provides the energy needed for assembly of the DNA-PKcs complex. Future studies will elucidate this possibility.

The DNA-PK complex may inhibit or promote apoptosis depending on the interacting proteins. Hence, regulation by proteins that are not part of the complex needs elucidation [20]. Together our findings suggest a role for TRIP13 in cell survival via enhanced NHEJ.

HR is error-free and essential for accurate transmission of genetic information. In contrast, NHEJ is error-prone, leading to mutations and cancer [6]. In our study, downregulation of TRIP13 led to a small increase of HR in BRCA1-deficient cells, likely due to functional BRCA2 in these cells. BRCA2, though not the primary transporter of RAD51, can bind and transport RAD51 to facilitate HR [44].

Radiation and chemotherapy, standard treatment for advanced SCCHN, promote apoptosis by inducing DSBs. Due to minimal improvement in patient survival in five decades, the

emphasis has moved to dose escalation. However, toxic effects on patients limit the extent to which radiation and chemotherapy can be intensified. Disruption of NHEJ promotes treatment sensitivity (apoptosis) whereas robust repair mediates treatment resistance (cell survival) [45, 46] and poor clinical outcome. Moreover, since NHEJ occurs without a DNA template, chromosomal aberrations develop. Therefore, treatment that induces DSBs in cells with robust NHEJ leads to secondary malignancies, further decreasing patient survival [47]. In fact, a recent study showed that overexpression of Ku80 correlated with treatment failure and poor survival in SCCHN patients [48]. Hence, inhibitors of NHEJ could improve patient survival. In the present study, we showed that knockdown of TRIP13 sensitizes SCCHN cells to radiation and chemotherapy. Moreover, TRIP13 sensitizes cells to the DNA-PKcs inhibitor Nu7026. These findings suggest a therapeutic strategy in tumors overexpressing TRIP13 (Fig 9).

Cisplatin-DNA adducts inhibit DNA-PKcs activity. TRIP13 overcomes this inhibition to promote NHEJ repair of DSBs by facilitating formation of the DNA-PKcs complex at the site of the break. Therefore, inhibition of TRIP13 in these tumors will sensitize them to the impact of cisplatin. Moreover TRIP13 overexpression induces DNA-PKCs phosphorylation (Ser2056) (Supplementary Fig 8B), and may play a critical role in combined therapies bypassing HR repair.

Cisplatin induces DNA-interstrand cross-links, which induce single strand breaks that are typically repaired by nucleotide excision repair. An important step in the repair of these crosslinks is DSBs. The lethality of cisplatin is reduced by efficient repair of DSBs by mechanisms such as NHEJ. Our data support that TRIP13 mediates DSB repair even when the HR is intact (Fig 6H), i.e. TRIP13 essentially hijacks repair to the NHEJ pathway. HR occurs during or immediately after DNA replication, in the S and G2 phases of the cell cycle when a template is available for repair. If the template is badly damaged or unavailable, HR repair cannot occur and the cell dies [45, 46].

In this study we showed that TRIP13 mediates classical NHEJ i.e. a prominent repair pathway in mammalian cells that is active throughout the cell cycle [49]. DSB repair may also occur via the alternative NHEJ (aNHEJ) or microhomology-mediated end joining pathway that was described more recently [50, 51]. The role of TRIP13, if any, in the aNHEJ pathway was not investigated. Although, initial studies suggested that aNHEJ occurs when classical NHEJ is deficient, more recent studies show that aNHEJ occurs even in cells with competent classical NHEJ [49]. In contrast to classical NHEJ, aNHEJ is infrequent and does not require Ku70, Ku80 and DNA-PKcs [49]. In this study, we showed that TRIP13 binds to proteins in this DNA-PK complex and facilitates DSB repair in SCCHN.

Thus, these studies define a new mechanism of treatment resistance and underscore the importance of targeting NHEJ to overcome treatment failure in SCCHN. Given the overexpression of TRIP13 in several treatment-resistant cancers., this strategy will likely be important for multiple cancers.

METHODS

Oncomine Database

Meta-analysis of TRIP13 in multiple cancers was performed using Oncomine (http://Oncomine.org) for SCCHN datasets and graphed. Data set used for this study Cromer-Head-Neck [12], Estilo-Head-Neck [13], Ye-Head-Neck [14], Kuriakose-Head-Neck [15], Ginos-Head-Neck [16], Toruner-Head-Neck [17].

Cell Culture

SCCHN cell lines were cultured as described [52]. All UM-SCC cell lines were provided by T. Carey (University of Michigan), and OSCC3 was provided by P. Polverini (University of Michigan). Cell lines were genotyped by the Sequencing Core at the University of Michigan pre-and post-completion of studies. Genotype was verified against published sequences for UM-SCC cell lines [53] and OSCC3 was compared with an early passage (P2) of cells from source vial. OSCC3 cells were thought to be derived from a squamous cell carcinoma of the ventral tongue [54, 55] but HeLa cell contamination was recently identified [56]. Therefore, these cells may not be a pure SCCHN cell line. In this study, multiple cell lines and complementary approaches in different cell lines were used to elucidate the overall function of TRIP13. Primary oral keratinocytes were cultured according to the supplier's instructions (ScienCell Research Laboratories, Carlsbad, CA). NIH 3T3 cells were cultured in DMEM with 5% calf serum. HCC1937 cells were cultured in RPMI medium (Gibco #11875) with 10% FBS (Gibco, #16000) and 1% Penicillin and streptomycin. COS-1 cells were cultured in DMEM (Gibco, #11965) with 10% FBS supplemented with penicillin and streptomycin.

Q-RT-PCR

Human oral keratinocytes (HOK), immortalized human oral keratinocytes (HOK16B), and UM-SCC cell lines were grown to ~60% confluence and total RNA including microRNA was isolated using miRNAeasy kit (Qiagen, Valencia, CA). cDNA was synthesized from total RNA using SuperScript III (Invitrogen, Carlsbad, CA). Quantitative Real Time PCR was performed with Power SYBR Green Master Mix on an Applied Biosystems 7600HT Real Time PCR machine. Data were analyzed by relative quantification method with normalization to GAPDH and then to normal keratinocytes. The forward and reverse primers were TRIP13GE-FP and TRIP13GE-RP, listed in the Supplementary Table 4. Each sample was run in triplicate and the average fold change was determined.

Immunoblot Analysis

Immunoblots were performed as described [57, 58]. The primary antibodies were TRIP13 (1:3000, #19802-1-AP) from Proteintech, Chicago, IL, KU70 (1:1000, # AB1358), anti-phospho-H2AX(ser139) (γH2AX) (1:1000, #05–636) both from Millipore, Billerica, MA), KU80 (1:1000,#2180), DNA-PKcs (1:1000, #4602) anti-phospho-DNA-PKcs (Ser 2056) all from Cell Signaling Technology, Boston, MA, and Actin (1:3000, # 612656) from BD Biosciences, Franklin Lakes, NJ). Secondary antibodies were HRP-conjugated goat anti-rabbit IgG or goat anti-mouse IgG (Jackson Immuno Research Laboratories, West Grove, PA). For IP, TrueBlot secondary antibodies (eBioscience Rbt#18-8816, Mouse#18-8817) were used. Immunoreactive proteins were visualized by SuperSignal-West-Pico-

Chemiluminescent system (Pierce, Pittsburgh, PA). The uncropped scanned films with molecular weight reference are included in the Supplementary Figure 9 through 11 in sequence of appearance in the main text. Signal intensity was quantified using ImageJ software (http://rsbweb.nih.gov/ij/).

Gene Amplification (FISH)

Fluorescence-in-situ hybridization (FISH) hybridization was performed on genotyped SCCHN cell lines SCCHN TMA (US Biomax) using BAC clones (RP11-914L5- 5' clone; RP11-1040C13-3'clone) for the TRIP13 break-apart probe. BAC clones were selected from UCSC genome browser and purchased through BACPAC resources (Children's Hospital, Oakland, CA). Fluorescence images were captured using a high resolution CCD camera controlled by ISIS image processing software (Metasystems, Germany).

Immunohistochemistry

Immunostaining on formalin-fixed, paraffin embedded tissue and scoring of stain intensity was performed as described [59] on a SCCHN tissue microarray (US Biomax). TRIP13 antibody for immunohistochemical studies was from Atlas Antibodies/Sigma Aldrich (Sigma, St. Louis, MO). Mouse IgG was used as negative control. For analysis of TMA data, interpretation and scoring were performed by a board certified pathologist as described [58]. Multivariate analysis of TRIP13 activity was based on the Proportional Odds ordinal regression model. The analysis had intensity in the nucleus as the primary response variable, categorized as none, low, medium and high. Explanatory variables included cancer diagnosis (binary), TNM stage (ordinal, 4 categories), grade differentiation (ordinal, 3 categories), age (15–82) and gender (binary). Models were fit by maximizing the likelihood. Forward and stepwise variable selection procedures and the Likelihood Ration test were used to select the best model for the data and to test statistical hypotheses.

Cell Transfection and Transduction

TRIP13 was downregulated with TRIP13 siRNA (Dharmacon, Lafayette, CO; sequence of siRNA used is listed in Supplementary Fig 1C). For overexpression of TRIP13, UM-SCC-1 cells were transfected with pCMV6-Flag-TRIP13 or pCMV6-Flag control vector (Origene, Rockville, MD). For inducible TRIP13 downregulation, unique microRNA-30 based doxycycline inducible Expression Arrest TRIPZ Lentiviral shRNAmir constructs were purchased from Thermo Scientific Open Biosystem. Two distinct TRIPZ oligonucleotide constructs in pTRIPZ vector (V2THS-28289, V3THS-345136) and control scrambled-shRNA were used to make lentiviral particles in the University of Michigan Vector-Core. After standardization the lentiviral particles with V2THS-28289, were used for all experiments.

Proliferation and Invasion Assay

Cells were seeded at equal densities (2×10^4 for UM-SCC-22B, UM-SCC-5; and 1×10^4 for OSCC3 and COS-1) 24–48 hours post-transfection and counted at 1d, 3d and 5d. For CDDP-treated cells, 24–48hrs after transfection cells were treated with CDDP or Nu7026 at the appropriate IC_{50} for 2hrs. Viable, nonviable, and total cells were quantified by the

Countess assay system using trypan blue (Invitrogen, Carlsbad, CA). Any p-value, calculated using the student's t-test, less than 0.05 was accepted as significant.

Cell invasion was assessed 24–48 hours after transfection using the modified Boyden chamber assay with Transwell inserts (Corning, Lowell, MA) coated with Matrigel (BD Biosciences, Franklin Lakes, NJ), as described [52]. Control inserts, not coated with matrigel, were used as a control for migration. Any p-value, calculated using the student's t-test, less than 0.05 was accepted as significant.

Apoptosis

Apoptosis was measured using flow-cytometry [60] as well as TUNEL. For Flow cytometry cells were double-stained with FITC-labeled AnnexinV and propidium iodide using the FITC-AnnexinV Apoptosis Detection system (BD Biosciences, Franklin Lakes, NJ). For detection of DNA strand breaks, nicks in DNA were labeled with the DeadEnd Fluorometric TUNEL kit (Promega, Madison, WI) according to the manufacturer's instructions. Formalin-fixed, paraffin-embedded tissue from *in-vivo* experiments were analyzed for apoptosis using TUNEL assay and the percent of FITC-positive cells was calculated.

Cell Cycle Analysis

Synchronized cells were dislodged with enzyme-free cell dissociation buffer (Invitrogen, Carlsbad, CA), centrifuged at 500*g* at 4°C, washed once in PBS and counted and were resuspended at 1million/500μl ice-cold PBS and 4.5ml of ice cold 70% ethanol was added drop wise. Cells were then stored overnight at −20°C. Cells were centrifuged and washed once with PBS, stained with 20μg/ml propidium Iodide (Sigma, St Louis, MO) in PBS containing 0.1% Triton X-100 and 200μg/ml DNase-free RNaseA (Invitrogen, Carlsbad, CA) for 20 minutes at room temperature, and analyzed by flow cytometry. The DNA content ratio between G1 and G2 was calculated as 1.83 and used throughout each experiment.

In-vivo Mouse Xenograft Model

Stable inducible UM-SCC-22B-shTRIP13 as well as shcontrol cells were injected subcutaneously at bilateral sites in athymic nude mice (Ncr-nu/nu, age 4–6 weeks, male, n=10, 5 for each of the No-Dox and Dox treated group) at 1×10^6 cells per left and right sides of the back of the mice respectively according to the University of Michigan UCUCA-approved protocol [52]. Tumors were grown for 7 days. After 8d, five mice were administered normal water with 10% sucrose and the other 5 mice were given water containing 10% sucrose supplemented with 2mg/ml doxycycline. Tumors were monitored and measured daily. A linear mixed effects statistical model was used to analyze the data. A random mouse-specific intercept term was included to adjust for tumor size measurements made on xenografts in the same mouse. Model-based Wald Tests were used and a p-value <0.05 was considered to be significant. In the TRIP13 overexpression study, stably overexpressing UM-SCC-1-TRIP13 and control cells (2×10^6 cells per site of each cell type) were injected subcutaneously at bilateral sites in athymic nude mice (Ncr-nu/nu, age 4–6 weeks, male, n=10, 5 in each group).

Focus Formation

NIH3T3 cells were transfected using Lipofectamine 2000 (Invitrogen, Carlsbad, CA). After 72 hours cells were replated at ~1000 cells per 60 mm plate and grown for 10 days. After fixing and washing with PBS, cells were stained with 0.2% Crystal violet solution prepared in 70% ethanol. Foci were counted for each plate.

Chick Chorioallantoic Membrane (CAM) Assay

The CAM assay was performed as described [28]. Briefly, 3T3 cells stably expressing TRIP13 or control vector were seeded on the CAM of d10 chick embryos and incubated for three days. The CAMs were excised, sectioned, and stained with hematoxylin and eosin. Invasive islands were quantified from multiple fields and graphed after normalization to control vector. Similarly UM-SCC-1-TRIP13, TRIP13 mutants and control pCMV6 cells were seeded on the top of the CAM whenever needed and was treated with NU7026 after 24hr. p-values were calculated using the student's t-test and any p-value less than 0.05 was considered significant.

Migration Assay

Cells were plated at 95% density in triplicate. Twenty-four hours later, cells were serum starved for 6 hours, then treated with 25 mM of mitomycin C (Sigma, St Louis, MO) for 2 hours in serum-free conditions. Media was removed and a scratch was made with a 200μL pipette tip. Immediately after the scratch, complete media with 25 mM mitomycin C was added. 3 fields in each replicate were photographed at 0 = and = 24 hours. The area between the migration fronts was determined using ImagePro Plus 5.1 (Media Cybernetics Inc, Bethesda, MD) and the percentage migration at 24 hours was calculated.

Clonogenic Assay

Cells were irradiated at varying doses 24h post-seeding and colonies were grown for 7d-14d. After the appearance of colonies, cells were fixed with methanol containing crystal-violet and quantified as described [61].

DNA Fragmentation

DNA was isolated from cells 4h post-radiation using PureLink Genomic DNA Mini Kit (Invitrogen, Carlsbad, CA). DNA fragmentation was visualized by agarose gel electrophoresis stained with ethidium bromide.

Detection of Double Strand Breaks

Whole cell lysates were collected from the cells irradiated with 2Gy of ionizing radiation at varying time points. Lysates were immunoblotted with γH2AX antibody and actin as a loading control. Signal intensity was quantified and graphed over time. The number of γH2AX foci per cell was quantified in five fields in both NonTarget and siTRIP13. The average number of foci per cell was calculated and graphed. The student's t-test was used to calculate a p-value. A p-value less than 0.05 was accepted as significant.

Comet Assay

Neutral comet assay was performed with treated cells. Glass slides with embedded cells in agarose were lysed in buffer containing 2.25 M sodium chloride, 8.9mM Tris-HCl, 10% DMSO and 1% Triton X100 (pH=10) for 16h. Lysed cells were equilibrated in running buffer TBE, electrophoresed and stained with Hoechst (Hoechst 33342, Invitrogen). After acquisition of images, the comet tail-moment was analyzed by the CometScore program.

Protein Purification and Mass Spectrometry

UM-SCC-1-FLAG-TRIP13 cells were used for TRIP13 protein purification by anti-Flag-M2 affinity gel (Sigma, #A2220) and Flag-tagged protein was eluted with flag peptide. Lanes corresponding to control and TRIP13-flag were cut into 15 slices and destained with 30% methanol for 4hrs. Upon reduction (10mM DTT) and alkylation (65mM 2-chloroacetamide) of the cysteines, proteins were digested overnight with sequencing grade modified trypsin (Promega, Madison, WI). Resulting peptides were resolved on a nano-capillary reverse phase column (Picofrit Column, New Objective, Woburn, MA) using 1% acetic acid/ acetonitrile gradient at 300nl/min and directly introduced into a linear ion-trap mass spectrometer (LTQ Orbitrap XL, ThermoFisher). Data-dependent MS/MS spectra on the five most intense ions from each full MS scan were collected (relative CE ~35%). Proteins were identified by searching the data against UniProt Human database appended with decoy (reverse) sequences using X!Tandem/Trans-Proteomic Pipeline (TPP) software suite. All peptides and proteins with a peotideProphet and ProteinProphet probability score of >0.9 (fdr<2%) were considered positive identifications. Proteins found in the control lane were subtracted using in-house subtraction program and the remaining were considered as potential interactors.

Co-Immunoprecipitation

Immunoprecipitation of TRIP13 co-complex proteins was performed by Pierce Co-IP kit (ThermoFisher Scientific, Rockford, IL, #26149).

DSB repair assay

DNA DSB-repair assays were performed using chromosomally integrated reporter constructs for both HR or NHEJ [26]. Plasmids containing the HR or NHEJ cassettes were linearized by digesting with NheI endonuclease (New England BioLabs, Ipswich, MA) and gel purified using Qiagen gel extraction kit (Cat# 28704). 1ug of this plasmid was used to transfect HR deficient (BRCA1 mutant) cells, HCC1937, using the amaxa kit (Lonza, Allendale, NJ) with the U20 program. Cells were selected with G418 and maintained in the presence of 250ug of G418 in RPMI media containing 10% FBS and 1% Penicillin/ Streptomycin. HCC1937 cells stably transfected with HR or NHEJ cassettes were transfected with NT or siTrip13 siRNAs. 48 hours after transfection DSBs were induced by transfecting cells with 5ug I-SceI expression plasmid using the Amaxa kit, U20 program with 0.1ug of dsRed expression plasmid as transfection control. Three days after transfection, cells were analyzed by flow cytometry for efficiency of DSB-repair. GFP and dsRed expression plasmids were used as controls. The ratio of dsRed/GFP was calculated to

represent the amount of DNA repair occurring. The student's t-test was used to calculate p-values. A p-value less than 0.05 was accepted as significant.

End Joining Assay

Mini NHEJ– Whole Cell Extract (mNHEJ–WCE) preparation and in-vitro end Joining experiment was done according to [62]. Briefly cells were grown to 70–80% confluency after appropriate treatment and were collected by scraping in PBS. Cells were washed twice in PBS, pelleted and snap frozen on dry ice. Frozen cell pellets were resuspended in 2 packed cell volumes (PCV) of hypotonic lysis buffer (10mM Tris (pH 8), 1mM EDTA (pH 8), 5mM DTT) and incubated on ice for 20 minutes with repeated vortexing. Cells were centrifuged for 2 min at 800*g* and the supernatant was collected and stored on ice. The pellet was resuspended in 1 PCV of nuclear extract buffer (25mM Tris (pH 8), 1.5mM EDTA (pH 8), 330mM KCL) and incubated on ice for 20 min. Retained supernatant was added back, re-suspended well and centrifuged for 10 minutes at 16,500*g* at 4°C. The supernatant (mNHEJ-WCE) was quantified for total protein, adjusted for concentration, stored in small aliquots at −80°C after quick freezing in liquid nitrogen. Approximately 250ng of gel-purified pcDNA3.1 plasmid double-digested with XhoI/BamHI (to generate non cohesive end) was incubated with 25μg (5μl) of mNHEJ-WCE, and 0.25 units of T4 ligase as positive control in 50mM Tris (pH 7.5),10mM $MgCl_2$, 10 mM DTT, 1mM ATP, in a reaction volume of 25μl. The reaction was incubated at 37°C for 1hr. The reaction was stopped by adding 2.5μl of 0.5M EDTA and 2.5μl of 10% SDS., DNA was purified using the Qiagen PCR purification Kit and loaded onto a 0.8% agarose gel, stained with ethidium bromide. Recircularized DNA was visualized and photographed.

γH2AX and Rad51 Co-localization by Immunofluorescence

Cells were stained with RAD51 (1:500) and γH2AX antibody (1:1000) in 0.3% triton X-100 overnight at 4°C. Cells were washed and incubated with secondary antibodies sequentially and imaged on an Olympus BX-51 microscope at the Microscopy and Image Analysis Core (University of Michigan). The number of co-localized foci (orange) per cell was quantified from five fields of cells in both NonTarget and siTRIP13. The average number of foci per cell was graphed. The student's t-test was used to calculate a p-value. A p-value less than 0.05 was accepted as significant.

Half Maximal Inhibitory Concentration (IC_{50})

Cells were seeded at ~1×10^4 cells per well. For CDDP, cells were treated with varying concentrations ranging from 0–30μM, in triplicate for 2hrs. Cells were counted 72hrs later. Each concentration was graphed as a percent of control (0μM) and the dose at which only 50% of the cells survived was calculated. For NU7026, cells were treated with varying concentrations ranging from 0–15μM in triplicate for 72hrs. Each concentration was presented in a graph as a percent of the control (0μM) and the dose at which only 50% of the cells survived was calculated.

TRIP13 Mutant Construct

TRIP13-WalkerA (TRIP13^{G184A}) mutant was generated by site directed mutagenesis of the conserved WalkerA motif of TRIP13 at the region of (179)**G**PPGT**GK**T(186) using primers TRIP13WALKERAG184ASe and TRIP13WALKERAG184AAs. The two PCR fragments were generated using wild type TRIP13-cDNA as template and 1st primer set TRIPFullCloneOriFP and TRIP13WALKERAG184AAs and with 2nd primer set TRIP13WALKERAG184ASe and TRIPFullCloneOriRP. PCR condition were 95°C for 4 min, 55°C for 1min followed by 30 cycles of 95°C-30 sec, 55°C-30 sec, 70°C-1 min and two hold at 70°C-6 min and at 4°C-forever. The PCR fragments were gel-purified and used for a second PCR using equal molar ratios of each fragment and with two end primers, TRIPFullCloneOriFP and TRIPFullCloneOriRP. The PCR conditions were: 95°C for 6 min, 55°C for 6 min followed by 12 cycles of 95°C-30 sec, 55°C-30 sec, 70°C-1 min and two hold at 70°C-6 min and at 4°C-forever. The final full fragment was gel purified, double-digested with BamHI and XhoI and ligated to the pCMV6 vector. Similarly, theTRIP13 deletion mutant was generated by deleting 20 conserved amino acids (293–312) from the ATPase domain of TRIP13 using primers TRIP13AAADelFP and TRIP13AAADelRP with similar PCR conditions. All primers are listed in the Supplementary Table T4. The PCR amplification was performed with Hi-fidelity Taq polymerase (Invitrogen#11304-011)

Malachite Green ATPase assay

Malachite green assay was performed according to Lanzetta et al [63] for ATPase activity of wild type TRIP13 and mutant proteins. Malachite green dye was prepared by combining 30ml of 0.045% of Malachite green dye (Sigma#38800) in H_2O and 10ml of 4.2% Ammonium Molybdate (Sigma#A1343) in 4N HCl (Fisher#SA56-1) and 800μl of 1% Triton X-100. The dye was left at room temperature in dark for 1hand filtered through 0.45μm filter (Millipore#SLHA033SS). The dye was prepared freshly every time before the experiment. 34% citric acid was prepared in H_2O and filtered. One million of each control cells and cells overexpressing TRIP13 or mutant proteins in either transiently transfected in COS-1 cells or stably transfected in UM-SCC-1 cells, were lysed in 392μl of buffer containing 50mM Triethanolamine (TEA), 50mM KCl, 20mM MgCl2 (pH 7.5) and 6mM CHAPS and incubated on ice for 5 minutes with repeated brief vortexing. At the end of the incubation, 8μl of 100mM ATP was added (final 2mM) and mixed thoroughly. 50μl of this mixture was added immediately (0 time point) to 400μl of malachite green dye solution and incubated at room temperature for 1 min and stopped with 100μl of 34% citric acid and absorbance (A_{660}) was measured. Subsequent measurements were taken at 2 minute intervals till 12 minutes. Background was eliminated by subtracting A_{660} value from each with a blank absorbance with dye and the buffer. The protein content of cell lysates was quantified and ATPase activity was normalized per microgram of protein. Each experiment was performed three times with three replicates within each experiment.

Supplementary Material

Refer to Web version on PubMed Central for supplementary material.

ACKNOWLEDGEMENTS

Financial support: This work was supported by NIDCR DE022567, DE019513and DE018512 (NJD). This research was made possible, in part, by the use of the Cancer Center Flow-Cytometry Core which was supported by the National Institutes of Health to the University of Michigan's Cancer Center Support Grant (5P30CA46592).

We are grateful to Dr. V. Gorbunova, University of Rochester for providing us HR and NHEJ constructs and Dr. M. Jasin (Memorial Sloan Kettering Cancer Center) for the I-SceI plasmid. We acknowledge David Adams from University of Michigan flow cytometry core and University of Michigan Sequencing core, Microscopy and Image analysis Laboratory core and Vineeta Sharma for technical assistance.

REFERENCES

1. Leemans CR, Braakhuis BJ, Brakenhoff RH. The molecular biology of head and neck cancer. Nat Rev Cancer. 2011; 11:9–22. [PubMed: 21160525]
2. Jemal A, Siegel R, Xu J, Ward E. Cancer statistics, 2010. CA Cancer J Clin. 2010; 60:277–300. [PubMed: 20610543]
3. Chapman JR, Taylor MR, Boulton SJ. Playing the end game: DNA double-strand break repair pathway choice. Mol Cell. 2012; 47:497–510. [PubMed: 22920291]
4. Kass EM, Jasin M. Collaboration and competition between DNA double-strand break repair pathways. FEBS Lett. 2010; 584:3703–3708. [PubMed: 20691183]
5. Jeggo PA, Lobrich M. DNA double-strand breaks: their cellular and clinical impact? Oncogene. 2007; 26:7717–7719. [PubMed: 18066083]
6. Collis SJ, DeWeese TL, Jeggo PA, Parker AR. The life and death of DNA-PK. Oncogene. 2005; 24:949–961. [PubMed: 15592499]
7. Bhalla N, Dernburg AF. A conserved checkpoint monitors meiotic chromosome synapsis in Caenorhabditis elegans. Science. 2005; 310:1683–1686. [PubMed: 16339446]
8. Wu HY, Burgess SM. Two distinct surveillance mechanisms monitor meiotic chromosome metabolism in budding yeast. Curr Biol. 2006; 16:2473–2479. [PubMed: 17174924]
9. Li XC, Bolcun-Filas E, Schimenti JC. Genetic evidence that synaptonemal complex axial elements govern recombination pathway choice in mice. Genetics. 2011; 189:71–82. [PubMed: 21750255]
10. Li XC, Schimenti JC. Mouse pachytene checkpoint 2 (trip13) is required for completing meiotic recombination but not synapsis. PLoS Genet. 2007; 3:e130. [PubMed: 17696610]
11. Agrawal N, et al. Exome sequencing of head and neck squamous cell carcinoma reveals inactivating mutations in NOTCH1. Science. 2011; 333:1154–1157. [PubMed: 21798897]
12. Cromer A, et al. Identification of genes associated with tumorigenesis and metastatic potential of hypopharyngeal cancer by microarray analysis. Oncogene. 2004; 23:2484–2498. [PubMed: 14676830]
13. Estilo CL, et al. Oral tongue cancer gene expression profiling: Identification of novel potential prognosticators by oligonucleotide microarray analysis. BMC cancer. 2009; 9:11. [PubMed: 19138406]
14. Ye H, et al. Transcriptomic dissection of tongue squamous cell carcinoma. BMC genomics. 2008; 9:69. [PubMed: 18254958]
15. Kuriakose MA, et al. Selection and validation of differentially expressed genes in head and neck cancer. Cellular and molecular life sciences : CMLS. 2004; 61:1372–1383. [PubMed: 15170515]
16. Ginos MA, et al. Identification of a gene expression signature associated with recurrent disease in squamous cell carcinoma of the head and neck. Cancer Res. 2004; 64:55–63. [PubMed: 14729608]
17. Toruner GA, et al. Association between gene expression profile and tumor invasion in oral squamous cell carcinoma. Cancer Genet Cytogenet. 2004; 154:27–35. [PubMed: 15381369]
18. Eymin B, Leduc C, Coll JL, Brambilla E, Gazzeri S. p14ARF induces G2 arrest and apoptosis independently of p53 leading to regression of tumours established in nude mice. Oncogene. 2003; 22:1822–1835. [PubMed: 12660818]

19. Shih C, Padhy LC, Murray M, Weinberg RA. Transforming genes of carcinomas and neuroblastomas introduced into mouse fibroblasts. Nature. 1981; 290:261–264. [PubMed: 7207618]
20. Li AY, et al. Suppression of nonhomologous end joining repair by overexpression of HMGA2. Cancer Res. 2009; 69:5699–5706. [PubMed: 19549901]
21. Fernandez-Capetillo O, Allis CD, Nussenzweig A. Phosphorylation of histone H2B at DNA double-strand breaks. J Exp Med. 2004; 199:1671–1677. [PubMed: 15197225]
22. Neuwald AF, Aravind L, Spouge JL, Koonin EV. AAA+: A class of chaperone-like ATPases associated with the assembly, operation, and disassembly of protein complexes. Genome Res. 1999; 9:27–43. [PubMed: 9927482]
23. Adamo A, et al. Preventing nonhomologous end joining suppresses DNA repair defects of Fanconi anemia. Mol Cell. 2010; 39:25–35. [PubMed: 20598602]
24. Muntean AG, et al. The PAF complex synergizes with MLL fusion proteins at HOX loci to promote leukemogenesis. Cancer Cell. 2010; 17:609–621. [PubMed: 20541477]
25. Nesvizhskii AI, Keller A, Kolker E, Aebersold R. A statistical model for identifying proteins by tandem mass spectrometry. Anal Chem. 2003; 75:4646–4658. [PubMed: 14632076]
26. Seluanov A, Mao Z, Gorbunova V. Analysis of DNA double-strand break (DSB) repair in mammalian cells. J Vis Exp. 2010
27. Ding J, Miao ZH, Meng LH, Geng MY. Emerging cancer therapeutic opportunities target DNA-repair systems. Trends Pharmacol Sci. 2006; 27:338–344. [PubMed: 16697054]
28. Liu M, et al. The Histone Methyltransferase EZH2 Mediates Tumor Progression on the Chick Chorioallantoic Membrane Assay, a Novel Model of Head and Neck Squamous Cell Carcinoma. Transl Oncol. 2013; 6:273–281. [PubMed: 23730406]
29. Tome S, et al. MSH2 ATPase domain mutation affects CTG*CAG repeat instability in transgenic mice. PLoS Genet. 2009; 5:e1000482. [PubMed: 19436705]
30. Karata K, Inagawa T, Wilkinson AJ, Tatsuta T, Ogura T. Dissecting the role of a conserved motif (the second region of homology) in the AAA family of ATPases. Site-directed mutagenesis of the ATP-dependent protease FtsH. J Biol Chem. 1999; 274:26225–26232. [PubMed: 10473576]
31. Urba S, et al. Single-cycle induction chemotherapy selects patients with advanced laryngeal cancer for combined chemoradiation: a new treatment paradigm. J Clin Oncol. 2006; 24:593–598. [PubMed: 16380415]
32. Carter SL, Eklund AC, Kohane IS, Harris LN, Szallasi Z. A signature of chromosomal instability inferred from gene expression profiles predicts clinical outcome in multiple human cancers. Nat Genet. 2006; 38:1043–1048. [PubMed: 16921376]
33. Kang JU, Koo SH, Kwon KC, Park JW, Kim JM. Gain at chromosomal region 5p15.33, containing TERT, is the most frequent genetic event in early stages of non-small cell lung cancer. Cancer Genet Cytogenet. 2008; 182:1–11. [PubMed: 18328944]
34. Rhodes DR, et al. Large-scale meta-analysis of cancer microarray data identifies common transcriptional profiles of neoplastic transformation and progression. Proc Natl Acad Sci U S A. 2004; 101:9309–9314. [PubMed: 15184677]
35. Tipton AR, Wang K, Oladimeji P, Sufi S, Gu Z, Liu ST. Identification of novel mitosis regulators through data mining with human centromere/kinetochore proteins as group queries. BMC Cell Biol. 2012; 13:15. [PubMed: 22712476]
36. Larkin SE, et al. Identification of markers of prostate cancer progression using candidate gene expression. Br J Cancer. 2012; 106:157–165. [PubMed: 22075945]
37. van Kester MS, et al. A meta-analysis of gene expression data identifies a molecular signature characteristic for tumor-stage mycosis fungoides. J Invest Dermatol. 2012; 132:2050–2059. [PubMed: 22513784]
38. Wojtasz L, et al. Mouse HORMAD1 and HORMAD2, two conserved meiotic chromosomal proteins, are depleted from synapsed chromosome axes with the help of TRIP13 AAA-ATPase. PLoS Genet. 2009; 5:e1000702. [PubMed: 19851446]
39. Zanders S, Sonntag Brown M, Chen C, Alani E. Pch2 modulates chromatid partner choice during meiotic double-strand break repair in Saccharomyces cerevisiae. Genetics. 2011; 188:511–521. [PubMed: 21515575]

40. Cahill D, Connor B, Carney JP. Mechanisms of eukaryotic DNA double strand break repair. Front Biosci. 2006; 11:1958–1976. [PubMed: 16368571]
41. Joyce EF, McKim KS. Drosophila PCH2 is required for a pachytene checkpoint that monitors double-strand-break-independent events leading to meiotic crossover formation. Genetics. 2009; 181:39–51. [PubMed: 18957704]
42. San-Segundo PA, Roeder GS. Pch2 links chromatin silencing to meiotic checkpoint control. Cell. 1999; 97:313–324. [PubMed: 10319812]
43. Shahi A, et al. Mismatch-repair protein MSH6 is associated with Ku70 and regulates DNA double-strand break repair. Nucleic Acids Res. 2011; 39:2130–2143. [PubMed: 21075794]
44. Holloman WK. Unraveling the mechanism of BRCA2 in homologous recombination. Nat Struct Mol Biol. 2011; 18:748–754. [PubMed: 21731065]
45. Ohnishi T, Mori E, Takahashi A. gH2AX. 2008 Springer;
46. Britten, RA. Modification of Radiosensitivity Following Chemotherapy Exposure : Potential Implications for Combined-Modality Therapy. Kluwer Academic Publishers; 2002.
47. Adachi N, Ishino T, Ishii Y, Takeda S, Koyama H. DNA ligase IV-deficient cells are more resistant to ionizing radiation in the absence of Ku70: Implications for DNA double-strand break repair. Proc Natl Acad Sci U S A. 2001; 98:12109–12113. [PubMed: 11593023]
48. Moeller BJ, et al. DNA repair biomarker profiling of head and neck cancer: Ku80 expression predicts locoregional failure and death following radiotherapy. Clin Cancer Res. 2011; 17:2035–2043. [PubMed: 21349997]
49. Deriano L, Roth DB. Modernizing the nonhomologous end-joining repertoire: alternative and classical NHEJ share the stage. Annual review of genetics. 2013; 47:433–455.
50. Guirouilh-Barbat J, Rass E, Plo I, Bertrand P, Lopez BS. Defects in XRCC4 and KU80 differentially affect the joining of distal nonhomologous ends. Proc Natl Acad Sci U S A. 2007; 104:20902–20907. [PubMed: 18093953]
51. Haber JE. Alternative endings. Proc Natl Acad Sci U S A. 2008; 105:405–406. [PubMed: 18180452]
52. Banerjee R, et al. The tumor suppressor gene rap1GAP is silenced by miR-101-mediated EZH2 overexpression in invasive squamous cell carcinoma. Oncogene. 2011; 30:4339–4349. [PubMed: 21532618]
53. Brenner JC, et al. Genotyping of 73 UM-SCC head and neck squamous cell carcinoma cell lines. Head Neck. 2010; 32:417–426. [PubMed: 19760794]
54. Lingen MW, Polverini PJ, Bouck NP. Retinoic acid induces cells cultured from oral squamous cell carcinomas to become anti-angiogenic. Am J Pathol. 1996; 149:247–258. [PubMed: 8686749]
55. Fischbach C, et al. Engineering tumors with 3D scaffolds. Nature methods. 2007; 4:855–860. [PubMed: 17767164]
56. Amornphimoltham P, et al. Rab25 regulates invasion and metastasis in head and neck cancer. Clin Cancer Res. 2013; 19:1375–1388. [PubMed: 23340300]
57. Mitra RS, et al. Rap1GAP promotes invasion via induction of matrix metalloproteinase 9 secretion, which is associated with poor survival in low N-stage squamous cell carcinoma. Cancer Res. 2008; 68:3959–3969. [PubMed: 18483282]
58. Zhang Z, et al. Rap1GAP inhibits tumor growth in oropharyngeal squamous cell carcinoma. Am J Pathol. 2006; 168:585–596. [PubMed: 16436672]
59. Mitra RS, Zhang Z, Henson BS, Kurnit DM, Carey TE, D'Silva NJ. Rap1A and rap1B ras-family proteins are prominently expressed in the nucleus of squamous carcinomas: nuclear translocation of GTP-bound active form. Oncogene. 2003; 22:6243–6256. [PubMed: 13679863]
60. Banerjee R, Henson BS, Russo N, Tsodikov A, D'Silva NJ. Rap1 mediates galanin receptor 2-induced proliferation and survival in squamous cell carcinoma. Cell Signal. 2011; 23:1110–1118. [PubMed: 21345369]
61. Franken NA, Rodermond HM, Stap J, Haveman J, van Bree C. Clonogenic assay of cells in vitro. Nat Protoc. 2006; 1:2315–2319. [PubMed: 17406473]

62. Smeaton MB, Miller PS, Ketner G, Hanakahi LA. Small-scale extracts for the study of nucleotide excision repair and non-homologous end joining. Nucleic Acids Res. 2007; 35:e152. [PubMed: 18073193]

63. Lanzetta PA, Alvarez LJ, Reinach PS, Candia OA. An improved assay for nanomole amounts of inorganic phosphate. Anal Biochem. 1979; 100:95–97. [PubMed: 161695]

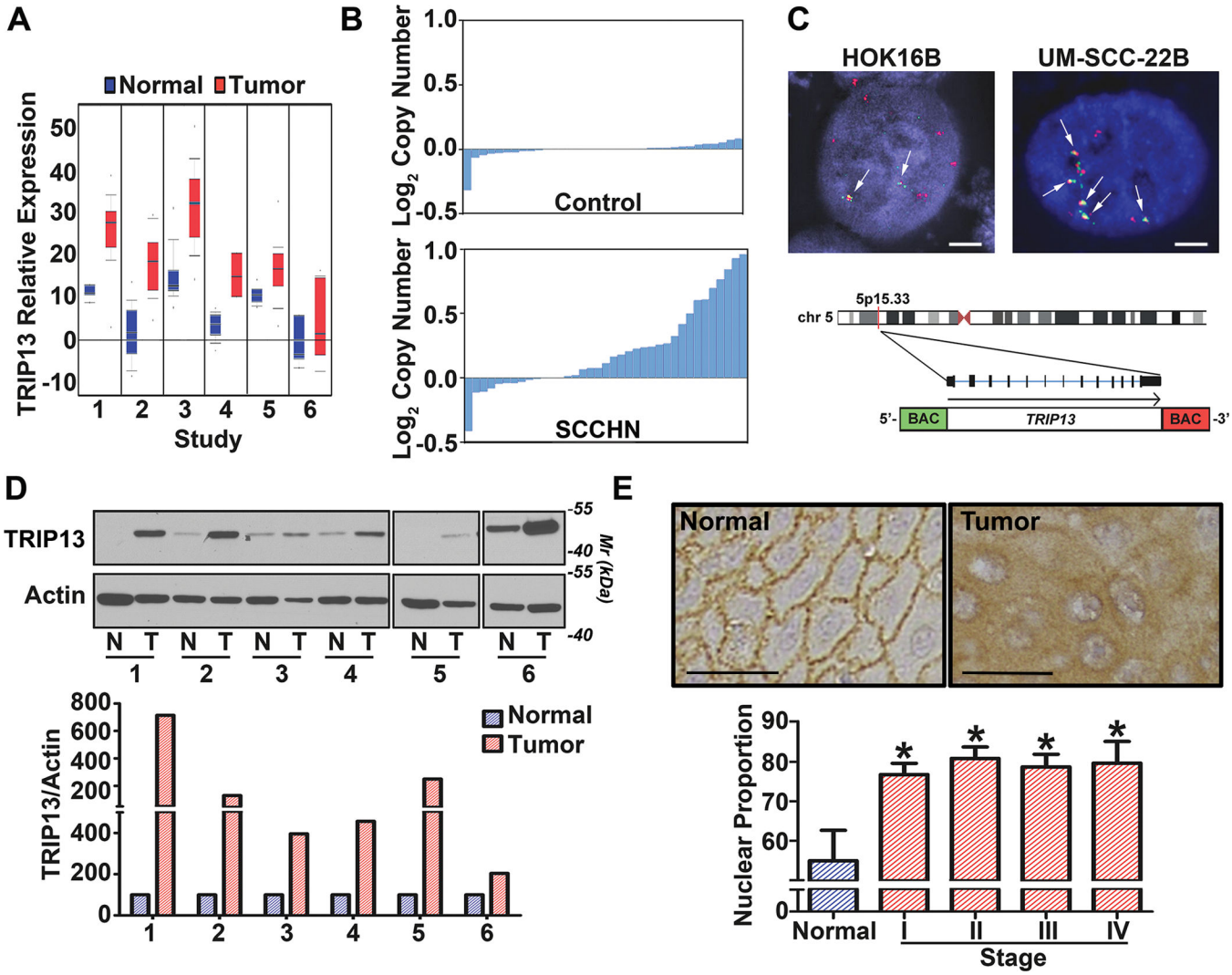

Figure 1. TRIP13 is upregulated in SCCHN

A) Meta-analysis showing TRIP13 upregulation in cancer compared to normal tissue. Left to right: Cromer-Head-Neck, Estilo-Head-Neck, Ye-Head-Neck, Kuriakose-Head-Neck, Ginos-Head-Neck, Toruner-Head-Neck (accession numbers are in Results section) B) Analysis of 35 normal and 37 SCCHN cases showing TRIP13 DNA copy number increase in TCGA dataset. C) FISH detection of *TRIP13* amplification in SCCHN cell line UM-SCC-22B compared to normal keratinocyte HOK16B. The 5' (green) and 3' (red) ends of *TRIP13* were labeled. Co-localization of 5' and 3' ends (yellow) indicates a full copy of *TRIP13* (white arrow) (bar=2μm). D) Matched normal and tumor tissue lysates from SCCHN patients were immunoblotted with anti-TRIP13 and anti-actin antibodies. Signal intensity was quantified (arbitrary-densitometric-units, DU), normalized to actin and expressed and plotted as percent of its corresponding control (lower panel). E) A TMA with SCCHN and normal tissue was stained for TRIP13 with DAB detection (bar=30μm). Staining proportion was scored and plotted (lower panel). Forward and stepwise variable selection procedures and the Likelihood Ration test were used for statistical analysis. ($p<0.05$).

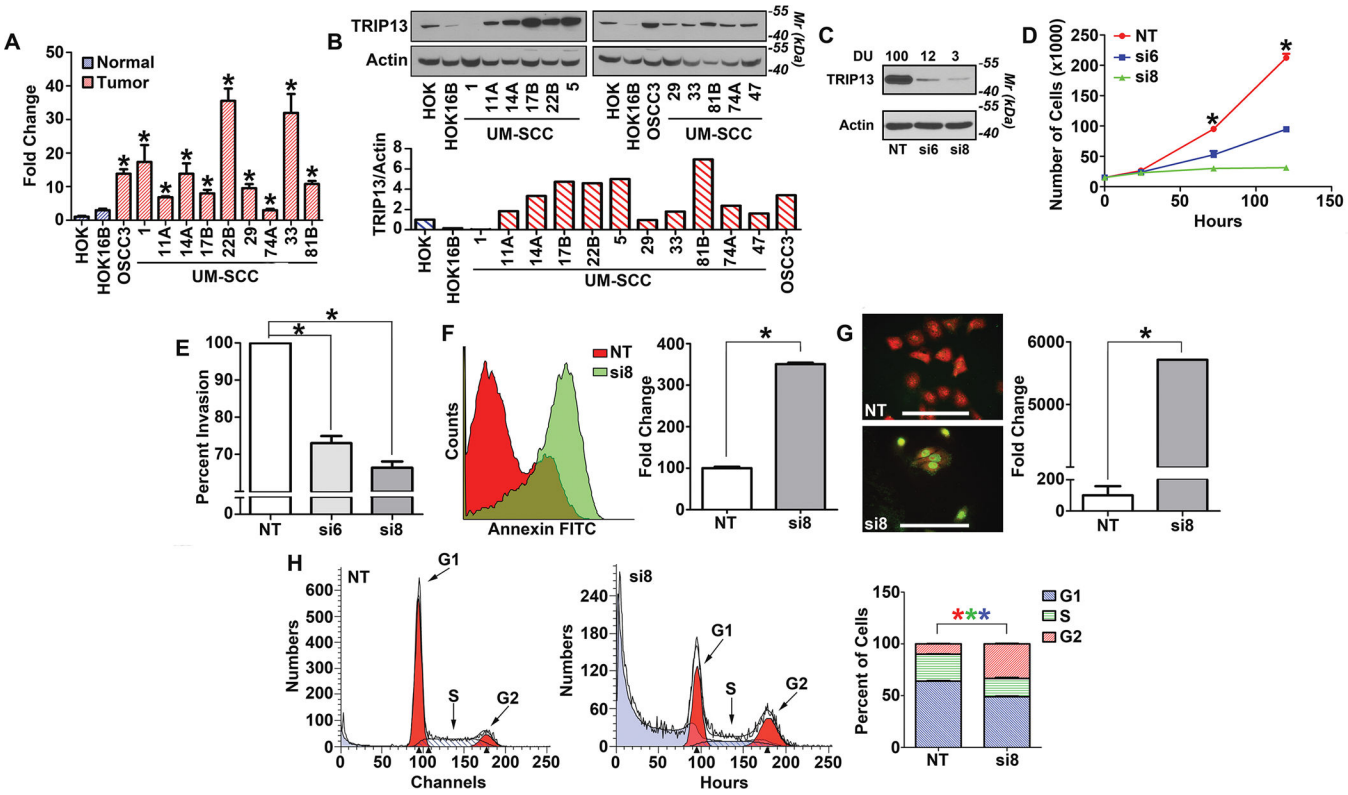

Figure 2. Suppression of TRIP13 inhibits oncogenic phenotypes

A) Total RNA from normal (HOK) and immortalized (HOK16B) keratinocytes and ten SCCHN cell lines was used for Q-RT-PCR. Data were normalized to GAPDH and then to normal keratinocytes. B) Lysates from SCCHN cell lines were immunoblotted with TRIP13 and actin. Signal intensity was quantified (DU), normalized to actin and plotted (lower panel). C) UM-SCC-22B cells were transfected with two different siTRIP13 (si6, si8) or Non-Target siRNA (siNT). After 72h cell lysates were immunoblotted with anti-TRIP13 and anti-actin. Signal intensity was normalized to actin and expressed as percent of control. D) Cells were transfected with siTRIP13 or control NT siRNA and seeded and counted (days 1, 3, 5) for proliferation assay. E) Cells were transfected with siTRIP13 or control NT siRNA and seeded on matrigel-coated inserts. Invasion was quantified at 48h post-seeding. F) Apoptosis was measured using flow cytometry and AnnexinV-FITC staining in cells transfected with siTRIP13-8 or control NT siRNA. G) Cells transfected with siTRIP13-8 or siNT were seeded on coverslips. Apoptosis was visualized by the TUNEL Assay (green cells). (bar=100μm). H) Cells, treated with siTRIP13-8 or siNT were synchronized and the distribution of cells in different phases of the cell cycle was determined by flow cytometry. Data represent three independent experiments performed in triplicate. (Student's t-test with SEM; $p<0.02$)

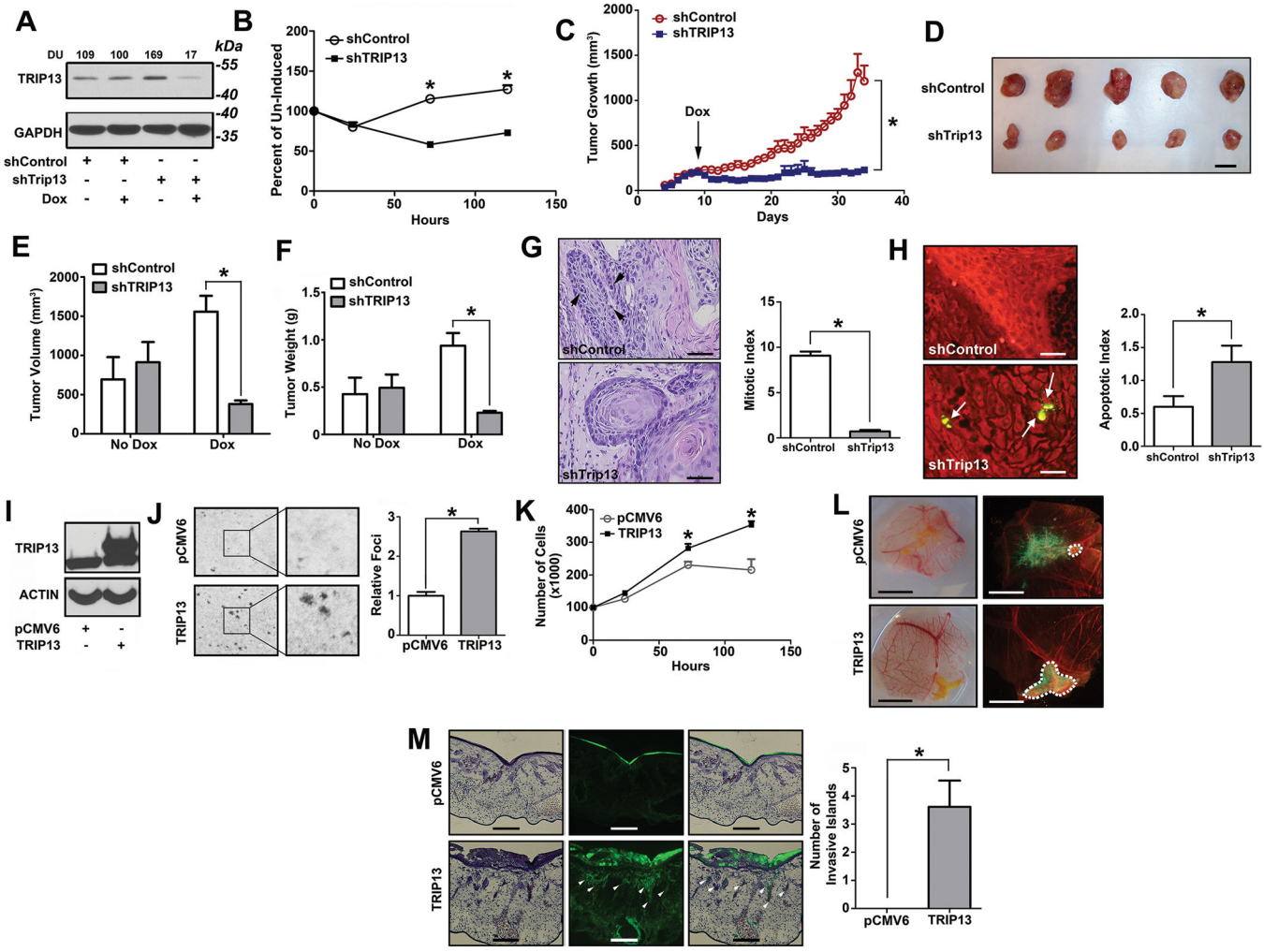

Figure 3. TRIP13 is oncogenic

A) UM-SCC-22B cells were stably transfected with inducible-shTRIP13 or shControl and lysates from doxycycline-induced and non-induced cells were immunoblotted with TRIP13 and actin antibodies. Signal intensity was quantified, normalized to actin and expressed as percent of induced-shControl. B) UM-SCC-22B-shControl and - shTRIP13 cells were seeded, induced with 1μg/ml doxycycline and counted. Data represent three independent experiments performed in triplicate. (Student's t-test with SEM; $p<0.03$). C) UM-SCC-22B-shControl and -shTRIP13 cells were injected subcutaneously into mice and induced with doxycycline after 8d. Tumors were measured daily for 34d. D) Gross appearance of tumors; shControl (upper) and shTRIP13 (lower) (bar=1cm). Volume E) and weight F) of shControl and shTRIP13 tumors +/− doxycycline. G) Mitoses/100 cells were quantified in 5 high-power-fields on tumor sections from these mouse xenograft tumors (bar=60μm). H) A TUNEL assay on tumor sections was performed. Apoptotic cells (green)/100 cells in 5 high-power-fields of each tumor were quantified (bar=25μm). I) NIH3T3 cells were transfected with pCMV6-Flag-TRIP13 or pCMV6-Flag. Cell lysates were immunoblotted with TRIP13 and actin antibodies. J) NIH3T3-pCMV6 and NIH3T3-TRIP13 cells were cultured for 14d, stained with crystal-violet, and foci were counted (4x inset expanded). Data represent three

independent experiments, each with three replicates. (Student's t-test with SEM; $p<0.04$). K) NIH3T3-pCMV6 and NIH3T3-TRIP13 cells cultured in a 24 well plate werecounted. Data represent one of three independent experiments, each with three replicates. (Student's t-test with SEM; $p<0.03$). L) NIH3T3 cells stably expressing TRIP13 and pCMV6 were seeded on the CAM of a 10d-old chick embryo and grown for 3d. Gross appearance of the tumors is shown (bar=5mm). M) Hematoxylin-eosin staining (left) and green fluorescent labeled cells (middle) and merged (right) panels show invasion of NIH3T3-TRIP13 cells (white arrow heads, bar=120μm). The number of invasive islands was calculated from 5 representative fields. (Student's t-test with SEM; $p<0.04$)

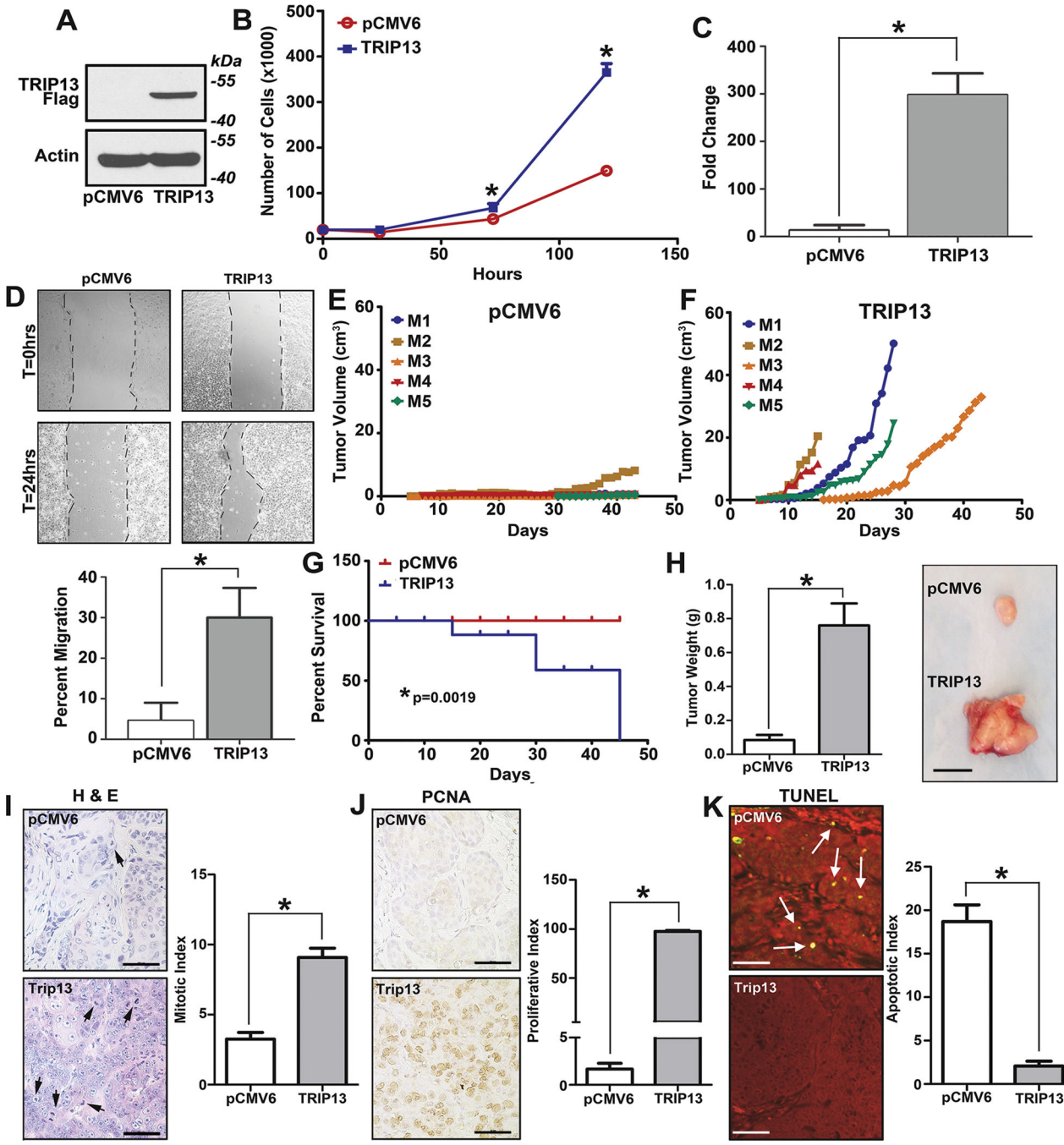

Figure 4. TRIP13 promotes tumor growth

UM-SCC-1 cells were stably transfected with pCMV6-Flag and pCMV6-Flag-TRIP13. A) Cell lysates were immunoblotted with anti-Flag and anti-actin antibodies. B) UM-SCC-1-pCMV6 and UM-SCC-1-TRIP13 cells were seeded and counted for proliferation. Data represent three independent experiments with three replicates in each experiment. (Student's t-test with SEM; $p<0.002$). C) UM-SCC-1-pCMV6 and UM-SCC-1-TRIP13 cells were seeded on matrigel-coated inserts and invasion was quantified 48h later. Data represent three independent experiments with three replicates in each experiment. (Student's t-test with

SEM; $p<0.002$). D) Cells were seeded at ~95% confluence and treated with mitomycin-C. After 24h, a scratch was performed and the migration distance was quantified (bottom panel). E) Stable UM-SCC-1-pCMV6 and F) UM-SCC-1-TRIP13 cells were injected subcutaneously in mice (n=5 in each group). Tumors were measured daily till mice were moribund. Tumor volume was calculated. G) Survival curves for mice injected with UM-SCC-1-pCMV6 or UM-SCC-1-TRIP13 were plotted. H) Tumor weight (left) and a representative xenograft-tumor from UM-SCC-1-pCMV6 and UM-SCC-1-TRIP13 (right) are shown (bar=1cm). I) Hematoxylin-eosin staining of xenograft-tumors and the mitotic index calculated from the average of all tumors (bar=60μm) (n=10, 5 in each group). J) Immunohistochemical staining of the xenograft-tumors with PCNA. Proliferative index represents the average staining in 100 cells in each of the tumors (bar=60μm). K) TUNEL staining was performed for detecting apoptotic cells. Apoptotic index represents the average number of apoptotic cells/100 cells in each of the tumors (bar=100μm). (Student's t-test with SEM; $p<0.05$).

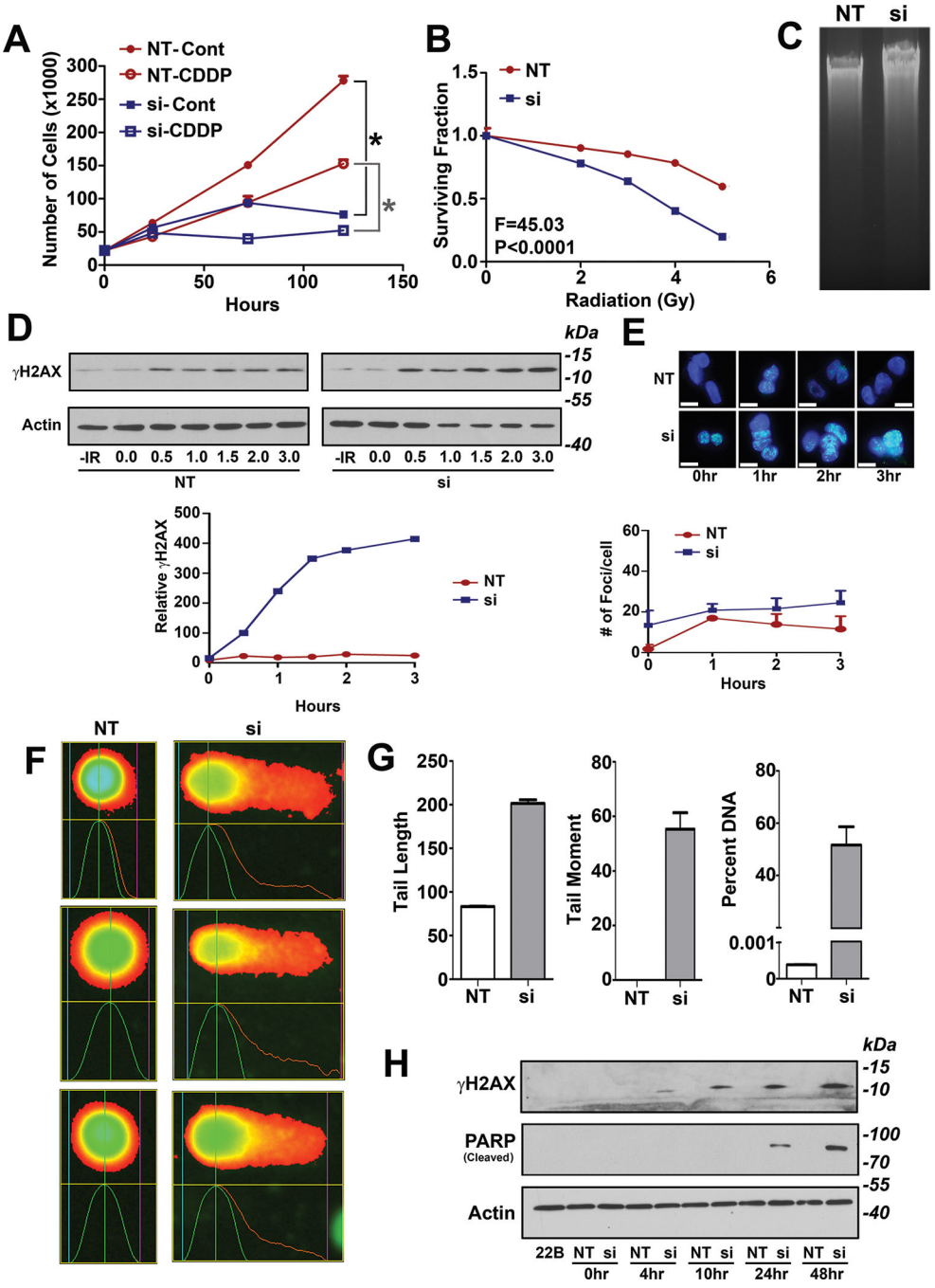

Figure 5. Suppression of TRIP13 increases DNA damage

UM-SCC-22B cells were transfected with siTRIP13 or siNT. A) Cells were treated with 5μM CDDP for 2h and counted 1d, 3d and 5d post-treatment. Data represent three independent experiments with three replicates in each experiment. (Student's t-test with SEM; $p<0.04$). B) Cells transfected with siNT or siTRIP13were seeded at siNT (3,000) and siTRIP13 (30,000) and 5d post-seeding, cells were irradiated (2, 3, 4 and 5Gy), then grown for 10d. Crystal-violet-stained colonies were counted. Data represent three independent experiments with three replicates in each experiment. C) Cells were synchronized with

nocodozole and irradiated (4Gy). Genomic DNA was isolated, electrophoresed and visualized with ethidium-bromide. D) Cells were irradiated (4Gy) and lysates were collected at 30m, 60m, 90m, 2h, 3h and 4h. Lysates were immunoblotted with anti-γH2AX and anti-actin antibodies. Signal intensity was quantified and plotted over time (bottom graph). E) Immunofluorescence with anti-γH2AX (green) and DAPI nuclear counterstain was performed after cells were irradiated (4Gy). The average number of γH2AX foci/cell was calculated for NT and siTRIP13 and plotted over time (bottom graph) (bar=20μm). F) Comet assay of cells transfected with siNT and siTRIP13 showing DNA damage (3 fields shown). G) Tail length, moment, and percent DNA in the tail were calculated. H) Time course of γH2AX and PARP cleavage were assessed with lysates prepared from UM-SCC-22B cells transfected with siNT and siTRIP13 and immunoblotted with anti-γH2AX, anti-cleaved-PARP and anti-actin antibodies.

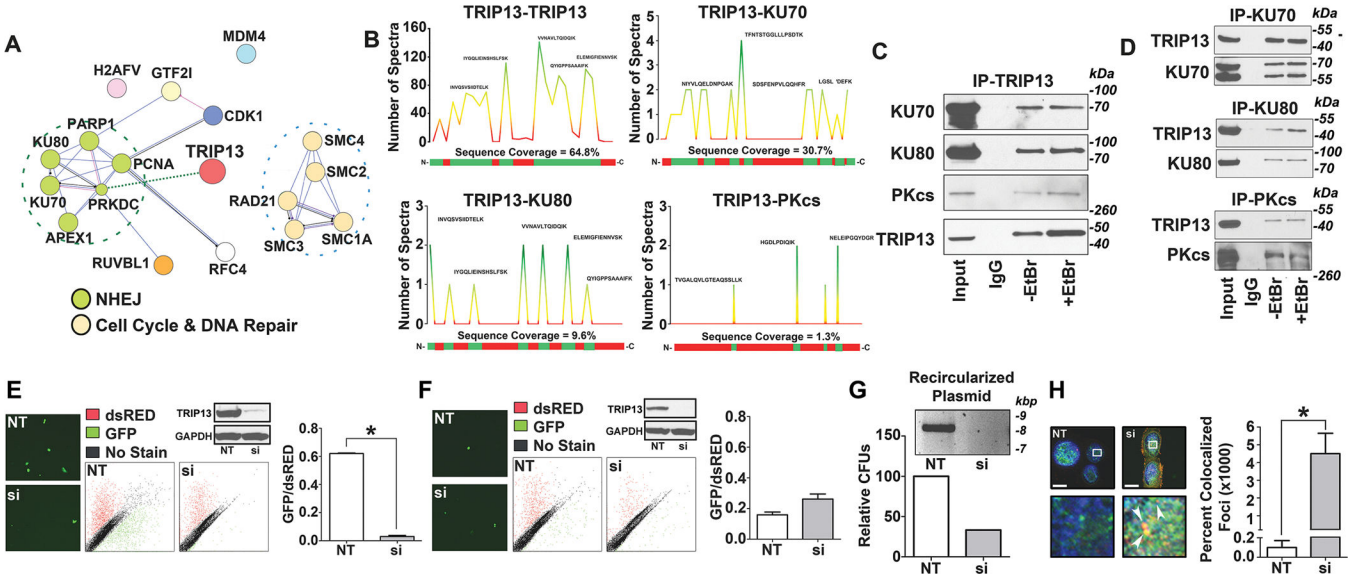

Figure 6. TRIP13 promotes NHEJ

A) Flag-tagged TRIP13 was purified from stable UM-SCC-1-TRIP13 and analyzed by mass spectrometry for TRIP13-binding proteins. An enrichment network, derived from string database of TRIP13-interactors that links NHEJ proteins as well as chromosomal integration and repair signatures. B) Peptide coverage for TRIP13 and TRIP13-interacting proteins for NHEJ pathway are shown. (C) TRIP13 was immunoprecipitated in the presence or absence of ethidium bromide and immunoblotted with anti-KU70, KU80, DNA-PKcs and TRIP13 antibodies. D) KU70, KU80 and DNA-PKcs were immunoprecipitated in the presence or absence of ethidium bromide with respective antibodies and immunoblotted with IP-antibodies and anti-TRIP13 antibody. E) HCC1937 cells stably expressing NHEJ (E) and HR (F) reporter constructs were transfected with siTRIP13 or NT. 48h later, these cells were co-transfected with dsRed and I-Sce-1 plasmids. NHEJ and HR were quantified by GFP and dsRed expression by flow-cytometry and quantified (right panel). G) Mini-NHEJ extract from UM-SCC-22B cells transfected with NT or siTRIP13 was incubated with linearized plasmid with non-cohesive ends. The end joining product (recircularized plasmid) was purified, electrophoresed and visualized with ethidium-bromide. Bacteria were transformed with re-circularized plasmid and colonies were counted (bottom graph). H) UM-SCC-22B-NT or -siTRIP13 cells were stained with γH2AX (green) and Rad51 (red) antibodies and DAPI (blue) (bar=20μm). Rad51/γH2AX co-localized foci (orange) (5X inset expanded) were quantified (right graph).

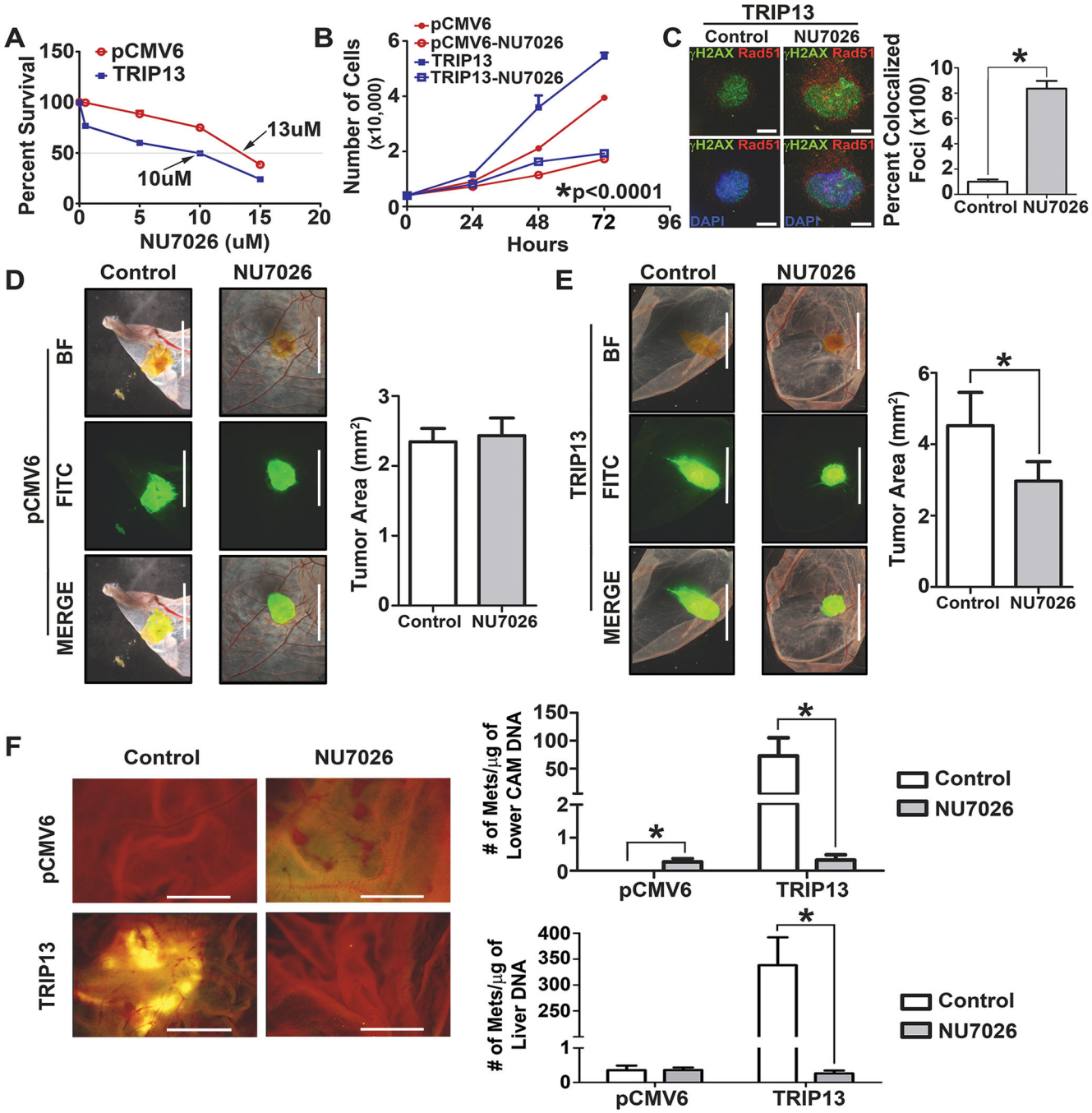

Figure 7. TRIP13 overexpression is sensitized to NHEJ protein DNA-PKcs

A) The IC_{50} for NU7026 in UM-SCC-1-pCMV6 (13μM) and -TRIP13 (10μM) cells were determined. B) UM-SCC-1-pCMV6 or -TRIP13 cells were seeded and 24h later were treated with 10μM NU7026 and subsequently cells were counted on 24h, 48h and 72h post NU7026 treatment. (Student's t-test with SEM; p<0.0001). C) UM-SCC-1-pCMV6 or -TRIP13 treated with 10μM NU7026 for 72h stained for γH2AX (green), Rad51 (red), and DAPI (blue) (bar=20μm). Co-localized foci (γH2AX/Rad51, orange) were quantified. Student's t-test with SEM; p<0.003). D, E) UM-SCC-1-pCMV6 (D) and UM-SCC-1-

TRIP13 (E) cells (1×10^6) were labeled with green Cell-tracker and seeded on the CAM of a 10d old chick embryo. 24h later, 200μM Nu7026 was added on top of the developing tumor. After 8d, the upper CAM was harvested, fixed and photographed (brightfield and GFP) and merged (bar=5mm). Tumor size was quantified (corresponding right graph, D and E). (Student's t-test with SEM; $p<0.05$). F) Metastasis to the lower CAM was evaluated by fluorescently labelled cells (left panel, bar=2mm) and metastasis in lower CAM and liver was determined by quantitative-Alu-PCR (right top and bottom panels respectively). (Student's t-test with SEM; $p<0.001$). Data is representative of two independent experiments, five replicates in each group.

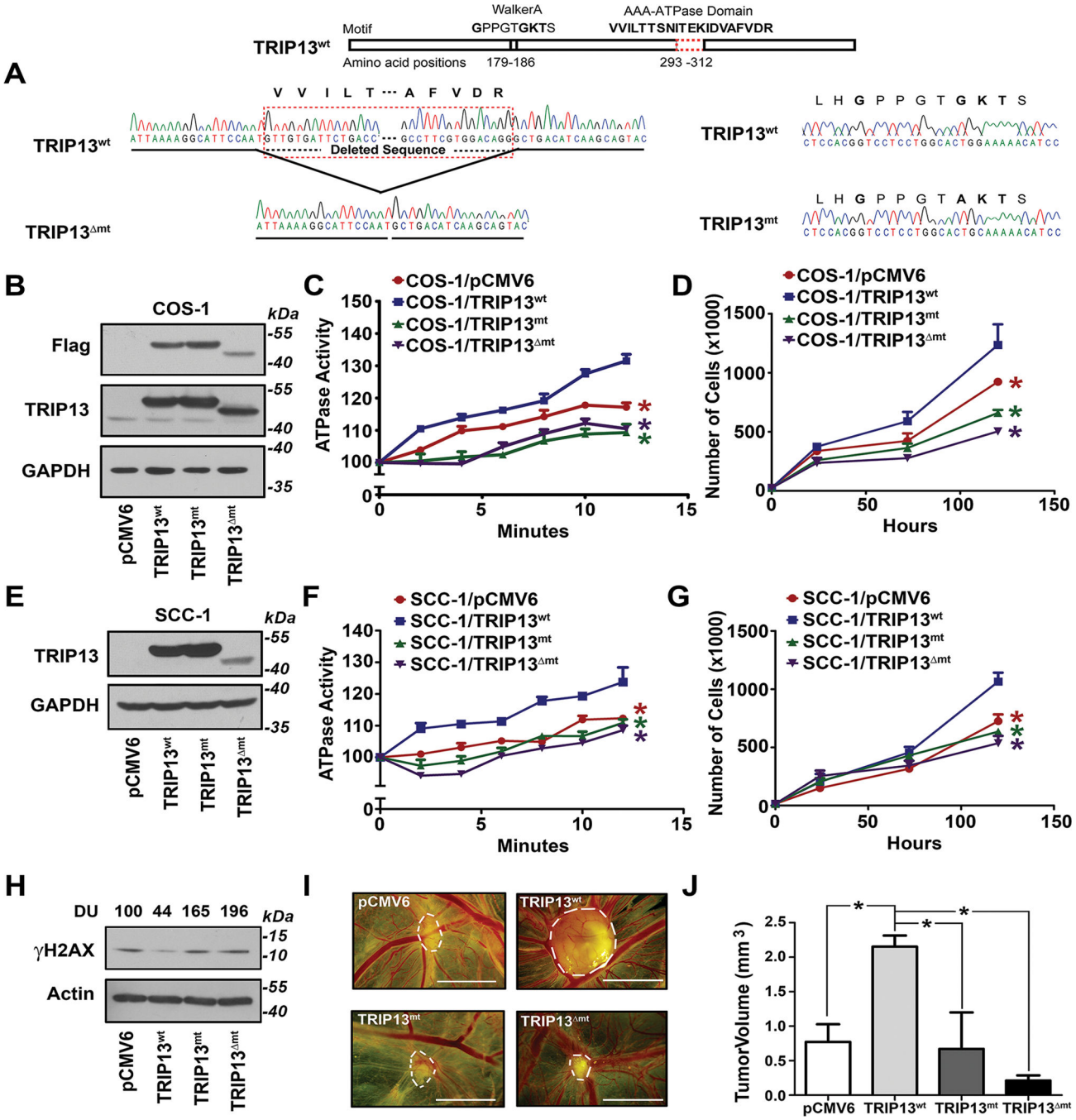

Figure 8. Mutation of the conserved domain of TRIP13 impairs tumorigenesis

A) Schematic presentation of conserved sequence motif of wild-type-TRIP13 (TRIP13^{wt}). The deleted and site-directed mutagenesis sites used for generation of TRIP13 mutants are shown. B) Expression of Flag tagged TRIP13 mutants was verified in COS-1 cells transiently overexpressing mutant proteins with antibodies to anti-Flag, anti-TRIP13 and anti-GAPDH antibodies. C) A malachite green ATPase activity assay was performed with TRIP13 mutant proteins as well as with wild type TRIP13 and pCMV6 control. ATPase activity was measured and normalized for 1μg of each protein and was finally expressed as

percent of corresponding activity at 0 minute time point and graphed. (Student's t-test with SEM; $p<0.04$). D) Proliferation assay was performed with COS-1 cells transiently overexpressing TRIP13 mutants. (Student's t-test with SEM; $p<0.02$). E) Expression of mutant or wild-type Flag-tagged TRIP13 in stably expressing UM-SCC-1 cells was verified with anti-TRIP13 and anti-GAPDH antibodies. F) A malachite green ATPase activity assay was performed with these cells. (Student's t-test with SEM; $p<0.05$). G) A proliferation assay was performed with UM-SCC-1 cells stably overexpressing mutant or wild type TRIP13 proteins along with control pCMV6 empty vector. (Student's t-test with SEM; $p<0.04$). H) UM-SCC-1 cells stably expressing wild type or mutant TRIP13 or control cells (pCMV6) were immunoblotted with anti-γH2AX, anti-actin antibodies and quantified (DU). I) Mixed clonal population of UM-SCC-1 cells stably expressing wild type or mutant TRIP13 or control cells were placed (1×10^6 cells each) on the CAM. After incubating for 7days, the upper CAM was excised and photographed (bar=5mm). The tumors (dotted boundary line) were measured and tumor volume was calculated (J). (Student's t-test with SEM; $p<0.01$).

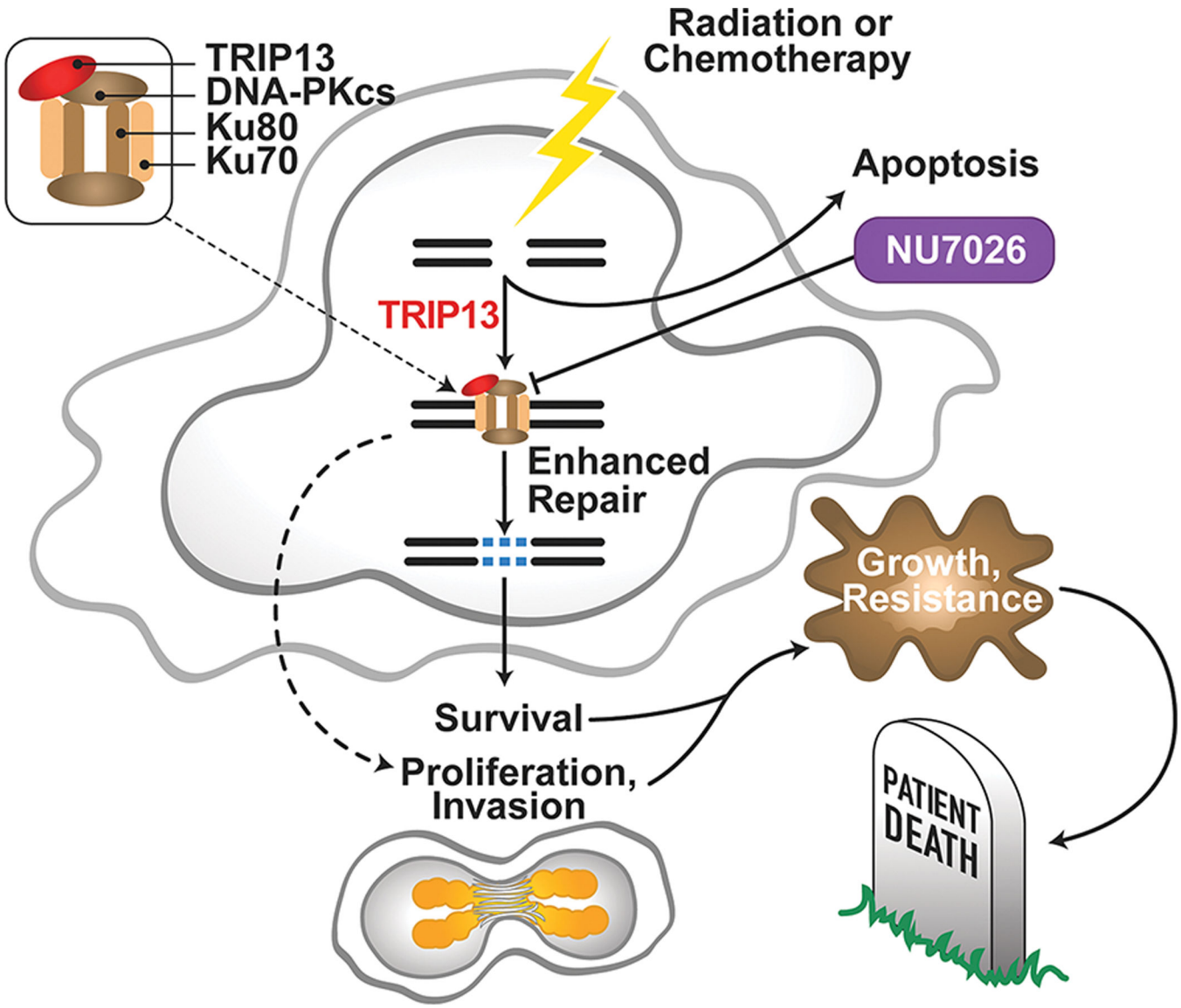

Figure 9. Proposed mechanism for TRIP13-mediated treatment resistance via enhanced DNA repair

In the presence of TRIP13, treatment-induced DSBs are robustly repaired via NHEJ leading to cell survival (treatment-resistance) and poor patient outcome in SCCHN. Tumors overexpressing TRIP13 are sensitive to NHEJ inhibitors (Nu7026).